ENSO Disrupts Boreal Winter CRE Feedback

Daeho Jin,[a,b] *Ryan J. Kramer,[a,b] Lazaros Oreopoulos,[b] and Dongmin Lee.[c,b]

[a] *GESTAR-II, University of Maryland – Baltimore County, Baltimore, MD, USA*

[b] *Earth Sciences Division, NASA's Goddard Space Flight Center, Greenbelt, MD, USA*

[c] *GESTAR-II, Morgan State University, Baltimore, MD, USA*

Corresponding author: Daeho Jin, Daeho.Jin@NASA.gov

*Current affiliation of Ryan J. Kramer: *Geophysical Fluid Dynamics Laboratory, NOAA, Princeton, NJ, USA*

ABSTRACT

Twenty years of satellite-based cloud and radiation observations allow us to examine the observed cloud radiative effect (CRE) feedback (i.e., CRE change per unit change in global mean surface temperature). By employing a decomposition method to separate the contribution of "internal changes" and "relative-frequency-of-occurrence (RFO) changes" of distinct cloud regime (CR) groups, notable seasonal contrasts of CRE feedback characteristics emerge.

Boreal winter CRE feedback is dominated by the positive shortwave CRE (SWCRE) feedback of oceanic low-thick clouds, due to their decreasing RFO as temperature rises. This signal is most likely due to El Niño-Southern Oscillation (ENSO) activity. When ENSO signals are excluded, boreal winter CRE feedback becomes qualitatively similar to the boreal summer feedback, where several CR groups contribute to the total CRE feedback more evenly.

Most CR groups' CRE feedbacks largely come from changing RFO: e.g., the predominant transition from oceanic cumulus to broken clouds and more occurrences of higher convective clouds with warming temperature. At the same time, low-thick and broken clouds experience optical thinning and decreasing cloud fraction, and these features are more prominent in boreal summer than winter. Overall, the seasonally asymmetric patterns of CRE feedback, primarily due to ENSO, introduce complexity in assessments of CRE feedback.

1. Introduction

Despite the importance of reliable global warming assessments, even the most sophisticated global climate models (GCMs) exhibit large uncertainties in simulating climate change. This is mainly due to the complex interactions among various components of Earth's climate system such as clouds, water vapor, snow/ice albedo and biogeochemistry (Forster et al. 2021). Among these factors, clouds and their radiative influence on Earth's energy balance is the largest source of uncertainty in warming projections (e.g., Kamae et al., 2016; Soden & Held, 2006; Zelinka et al., 2020).

Cloud feedbacks, namely the radiative response to global warming-induced cloud changes, are typically examined using numerical model experiments. For example, in the pioneering work by Wetherald & Manabe (1988), a set of experiments was used to assess the change of radiative fluxes in response to perturbations of specific variables. Later, Cess et al. (1990, 1996) performed experiments with perturbed sea surface temperatures (SSTs) and examined the role of clouds in radiative flux changes using the concept of cloud radiative effect, CRE, the difference between all-sky (including clouds) and clear-sky (cloudless) fluxes. However, it has become widely accepted that such a CRE based calculation is not the most accurate assessment of the narrowly defined cloud feedback, since it also includes the cloud masking of non-cloud changes which is not considered as cloud feedback per se (e.g., Zhang et al., 1994; Colman, 2003; Soden et al., 2004), as well as changes in clear-sky fluxes. These confounding factors, and the nonlinearity of cloud feedback, demand more sophisticated analyses such as those that can be achieved with the "radiative kernel" (Soden et al. 2008) and partial radiative perturbation (PRP) methods (Colman and McAvaney 1997; Wetherald and Manabe 1988). Radiative kernels have been used in GCMs to diagnose uncertainty in global-mean radiative forcing and feedbacks relevant for climate sensitivity (e.g., Smith et al., 2020; Soden et al., 2008) and the hydrological cycle (Myhre et al. 2018; O'Gorman et al. 2012), and also to understand the role of radiative changes in physical processes such as convective organization (Bony et al. 2020; Zhang et al. 2019).

To diagnose specifically cloud feedback, the concept of the "cloud radiative kernel (CRK)" was developed to capture the radiative effects of clouds whose populations are distributed in 2D joint histograms of cloud top pressure (CTP) and optical thickness (COT) (Zelinka et al. 2012a,b, 2016). Such histograms are prominently featured in International Satellite Cloud Climatology Project (ISCCP) observations (Rossow and Schiffer 1991, 1999) and their GCM simulators (Bodas-Salcedo et al. 2011; Klein and Jakob 1999; Webb et al. 2001). The CRK framework has advanced our understanding of what kind of cloud changes contribute to feedbacks. Recently Zelinka et al. (2022; Z22 hereinafter) reported further details of cloud feedbacks in GCMs by combining CRKs with model clouds assigned to ISCCP cloud regimes (Jakob and Tselioudis 2003; Rossow et al. 2005; Tselioudis et al. 2013, 2021). Z22 analyzed inter-regime and intra-regime responses to increased surface temperature, and found models to consistently simulate decreases of cloud amount and increases of cloud albedo with warming, and a thinning (thickening) of tropical (extratropical) clouds.

Observations from the Moderate Resolution Imaging Spectroradiometer (MODIS) and Clouds and the Earth's Radiant Energy System (CERES) sensors aboard the Terra and Aqua satellites are now available for more than 20 years, sufficient for examining trends in Earth's energy budget and role of cloud feedback. For example, Loeb et al. (2021) showed a notable positive trend of Earth's energy imbalance based on satellite observations, while Raghuraman et al. (2023) examined the offsetting effect of opposing longwave CRE (LWCRE) and shortwave CRE (SWCRE) trends contributing to near-zero trend of net CRE. In this study we examine the decomposition of cloud feedbacks by cloud regimes following Z22, but based solely on MODIS and CERES observations and without invoking CRKs. The objective is to examine cloud-related radiation changes contemporaneous with mean surface temperature change (i.e., CRE feedback), by applying Z22's concept of decomposing CRE changes to those due to within-regime cloud property changes and regime occurrence changes. Feedback characteristics are contrasted not only between land and ocean, but also between seasons, the latter examined to test the hypothesis that dramatically different seasonal distribution of clouds respond differently to global warming. Notably, the El Niño-Southern Oscillation (ENSO) activity strongly affecting global climate at interannual time scales is asymmetrically strong in boreal winter compared to boreal summer, thus necessitating a seasonal CRE feedback analysis.

2. Data and cloud regimes

a. Radiation flux and surface temperature

Radiative fluxes at the top-of-atmosphere (TOA) are obtained from the CERES Flux By Cloud Type (FBCT) product which is available daily at 1-deg resolution (Sun et al. 2022) and provides exact spatiotemporal matching with MODIS cloud regimes since it is based on MODIS radiances. The FBCT product comprises only daytime fluxes since it resolves fluxes in the COT-CTP phase space and COT is retrievable only during daytime. Clear-sky FBCT fluxes are missing for about 20% of grid cells on average due to either unavailable satellite observations or overcast conditions. We filled this missing data via linear interpolation in space and time. When we tested one of our key results with the more complete CERES Energy Balance and Filled (EBAF) monthly data (Loeb et al. 2018), we confirmed that our gap-filled FBCT data is reliable (see Section 3a).

The global surface temperature comes from MERRA-2 reanalysis (surface skin temperature [T_s]; Gelaro et al., 2017). We focus on 3-month means (December to February [DJF], and June to August [JJA]; a.k.a. seasonal means) for the period of December 2002 to August 2022 (20 seasons), in the "near-global" domain of 60°S-60°N. Area-weighted domain mean values are well-approximated by using cosine of latitude weights. When comparing the results based on MERRA-2 T_s with those based on Hadley Center sea ice and sea surface temperature (SST) dataset (HadISST; Rayner et al., 2003), we find the CRE feedback magnitudes generally larger for the latter, since SST variability is smaller than that of T_s, but conclusions are not affected. The *p*-value for regression analysis is calculated according to the effective degrees of freedom derived from auto- and cross-correlations (Afyouni et al. 2019).

b. Cloud regimes

The cloud classification is based on cloud regimes (CRs) obtained via *k*-means clustering of MODIS 2D joint histograms of COT and CTP (Collection 6.1; Platnick et al., 2017, 2018). While the clustering process used distinct Terra and Aqua joint histograms in the 50°S-50°N domain (at daily 1° resolution from June 2014 to May 2019; Jin et al. 2021), regime assignment for a particular grid cell was performed using the average Terra-Aqua joint histogram (TA_mean) in the extended 60°S-60°N domain from Sep. 2002 to Aug. 2022. This approach minimizes unassigned grid cells and ensures that the cloud classification represents daytime mean observations while utilizing the most available cloud observations. Details about the CRs are presented in the Appendix.

The full set of 17 CRs (including the sub-regimes) capture in great detail the characteristics of global cloudiness. However, for studying CRE feedback, this large number of CRs makes the analysis, interpretation of results, and presentation somewhat cumbersome. Hence, we proceeded to organize the CRs into 8 groups: tropical high thick (H1_tk) and thin (H1_tn) clouds, lower altitude high clouds that are mostly extratropical and were also divided into thick (H2_tk) and thin (H2_tn), mid-level clouds (Mid), thick (L_tk) and thin (L_tn) low clouds, and semi-clear clouds (S-Clr). The grid cells for which no CR was assigned (e.g., completely clear sky or missing in the MODIS dataset) are designated as "CS+Ms". The combined joint histogram of CR centroids and mean RFO map of CRs assigned to each group are shown in Fig. 1. CR members for each group and seasonal mean RFOs of the CR groups by land/ocean are provided in Table 1, indicating that seasonal differences in terms of mean

RFO are small. The seasonal mean properties of SWCRE and LWCRE are similar for the CRs within each group (Supplementary Fig. S1), affirming that the CR groups can serve as a representative summary of the individual CR behaviors. This figure shows that the largest absolute values of SWCRE/LWCRE correspond to H1_tk clouds, although the CRE contribution is dominated by S-Clr clouds because their RFO (about 40%) dwarfs those of all other CR groups (not shown).

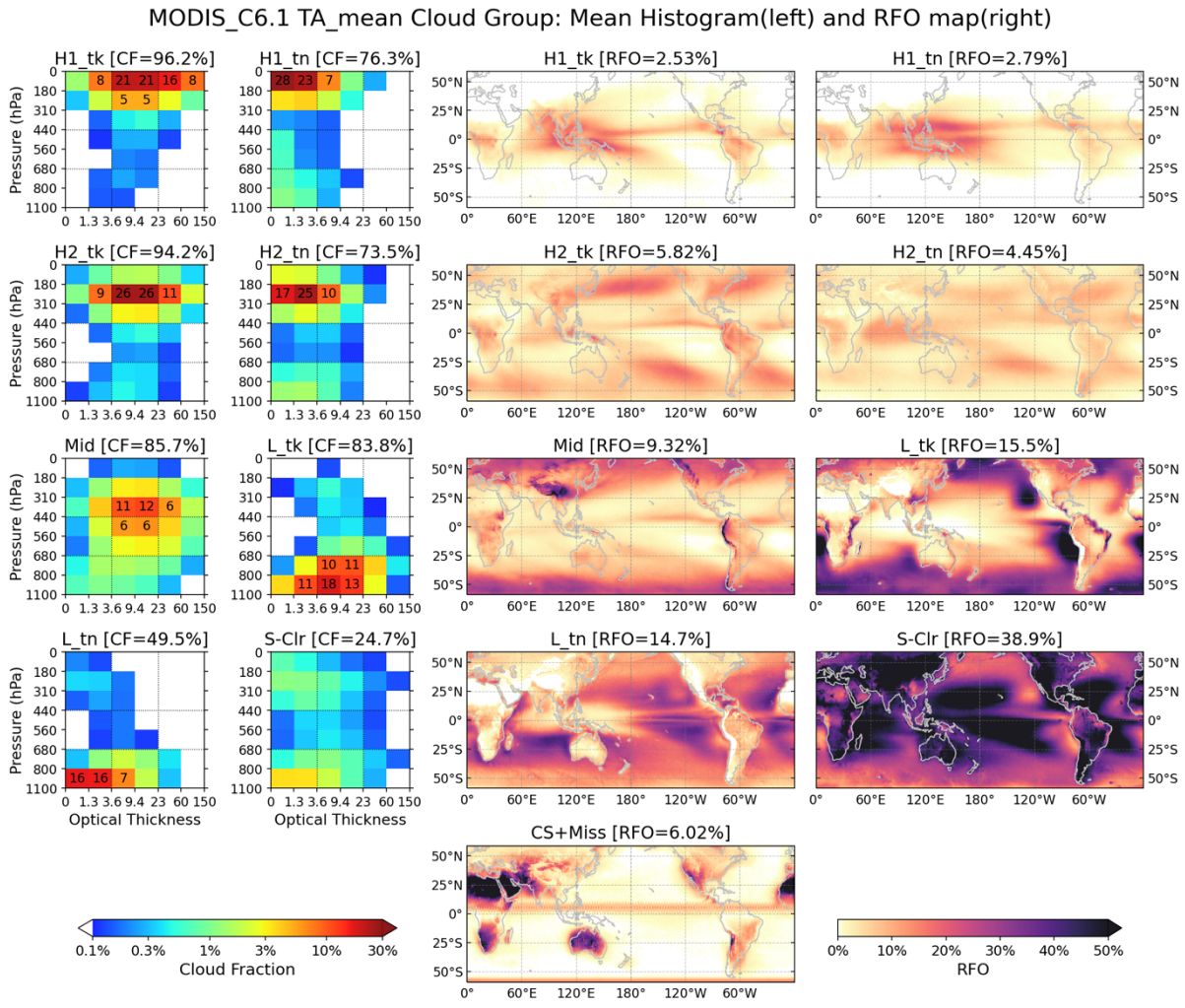

Fig. 1. (left) CR group mean joint histograms and (right) geographical distribution of relative frequency of occurrence (RFO) after Terra-Aqua mean (TA_mean) histograms were assigned into 60°S-60°N domain (2002.09-2022.08). The mean RFO provided above each map panel is obtained by using a cosine of latitude weight when averaging the RFO distribution (for consistency to temperature and radiation variables), and mean joint histograms are obtained from weighted average by mean RFO of each CR. Bin cloud fraction values exceeding 5% are shown explicitly on the joint histograms, with the total cloud fraction of each CR group also shown above each joint histogram.

158 Table 1. Area-weighted relative frequency of occurrence (RFO) within 60°S-60°N for our
159 cloud regime (CR) groups and the group of clear sky and missing joint histograms. The CRs
160 themselves are shown in the Appendix.

Full Name	Acronym	CR Member(s)	DJF			JJA		
			Ocean	Land	Total	Ocean	Land	Total
Tropical High & Thick clouds	H1_tk	1,3,5	1.96%	0.66%	2.62%	2.03%	0.68%	2.70%
Tropical High & Thin clouds	H1_tn	7,9	2.61%	0.51%	3.12%	2.16%	0.36%	2.52%
Extratropical high & Thick clouds	H2_tk	2,6	4.32%	1.57%	5.89%	3.95%	1.57%	5.52%
Extratropical high & Thin clouds	H2_tn	8	3.28%	1.03%	4.30%	3.30%	0.84%	4.14%
Mid-level clouds	Mid	4, 15A, 15B	6.70%	3.60%	10.30%	5.43%	3.01%	8.44%
Low & Thick clouds	L_tk	10,11,12, 13	13.36%	2.13%	15.49%	12.99%	2.57%	15.56%
Low & Thin clouds	L_tn	14	14.37%	1.11%	15.47%	12.20%	1.26%	13.47%
Semi-clear clouds	S-Clr	15C	25.49%	12.00%	37.49%	29.07%	11.46%	40.53%
Clear-sky & Missings	CS+Ms	N/A	1.52%	3.79%	5.31%	2.48%	4.63%	7.11%
Sum			73.6%	26.4%	100.0%	73.6%	26.4%	100.0%

161

162

163 ## 3. CRE feedbacks and their decomposition

164 *a. Seasonal mean CRE feedback*

165 In this study CRE feedback α is defined as in previous studies (e.g., Chung & Soden,
166 2018), with the CRE (X) and domain mean surface temperature (T_s):

167 $$\alpha = \frac{\partial X}{\partial T_s} \quad (1)$$

168 The value of α can be obtained by a linear regression of X against T_s.

169 $$X = \alpha \cdot T_s + \beta + \epsilon \quad (2)$$

170 $$where\ \beta = intercept, and\ \epsilon = residual$$

171 For this analysis, the β term is irrelevant and is ignored. Figure 2 shows the 20-year
172 distribution of seasonal and near-global mean SWCRE/LWCRE vs. T_s, and corresponding
173 linear regression lines for DJF and JJA. The variability of T_s is larger in DJF than JJA, while
174 that of SWCRE is similar in the two seasons, thus resulting in larger SWCRE feedback (=
175 steeper slope of regression line) in JJA (2.31 $Wm^{-2}K^{-1}$) than DJF (1.73 $Wm^{-2}K^{-1}$). The
176 regression slope of LWCRE is also steeper in JJA than DJF (-1.36 $Wm^{-2}K^{-1}$ vs. -0.54 $Wm^{-2}K^{-1}$
177). Positive SWCRE feedback means less outgoing SW radiation (less reflection) as surface
178 warms, and negative LWCRE feedback means more outgoing LW radiation with warming,
179 thus competing against each other. The correlations between CRE and T_s, are fairly strong
180 (coefficient magnitudes>0.57) with low p-values (<0.053) indicating that the relationships are
181 significant with high confidence except for LWCRE in DJF (r=-0.273; insignificant at the
182 90% confidence level). When comparing SWCRE and LWCRE, SWCRE is more strongly
183 correlated with DJF T_s while LWCRE is more strongly correlated with JJA T_s. We also
184 repeated this analysis for both seasons with CERES EBAF monthly data (Ed. 4.2;
185 Supplementary Fig. S2), and confirmed their consistency with these FBCT results. We find
186 these seasonal differences of SWCRE/LWCRE feedback signals to be mainly driven by El
187 Niño-Southern Oscillation (ENSO) which is more active in DJF (see Section 4a). It is worth
188 noting that the global warming trend in terms of T_s is more notable in JJA than DJF (Figs. 2c
189 and 2f) as indicated by the light color circles corresponding to later years congregating more
190 at higher temperatures (right side) in the former case.

191

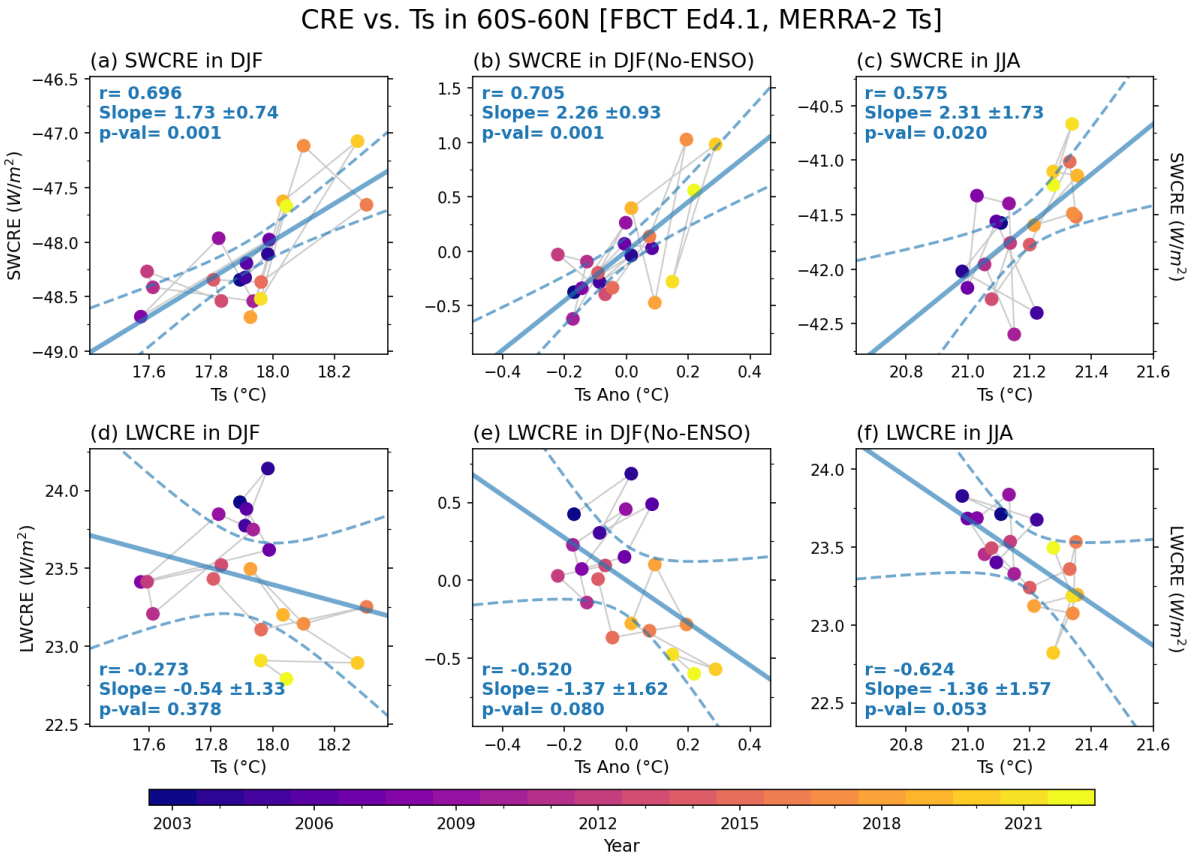

Fig. 2. (a), (b), (c) SWCRE vs. domain mean surface temperature (T_s) in 60°S-60°N for DJF, No-ENSO DJF, and JJA seasonal means, and (d), (e), (f) LWCRE vs. T_s. Blue solid lines are regression lines of SW/LWCRE against T_s and blue dash curves show 5% to 95% range of regression mean. Correlation coefficients (r), regression slope uncertainties in 5% to 95% range, and p-values are provided in each panel. Each year is represented by a different symbol color according to the color bar at the bottom and light gray lines connect consecutive year symbols.

b. Decomposition of CRE feedback by CR groups

Following Eq. 1 in Z22, the decomposition of CRE (X) by cloud regime (which also applies to our CR groups) is represented as:

$$X = \sum_{r=1}^{R} f_r X_r \quad (3)$$

where f_r and X_r represents the RFO and the average of X within the grid cells belonging to a group r. Similar to the linear regression in Eq. 2, a CR group's contribution to CRE can also be represented by a linear regression:

$$f_r X_r = \alpha_r \cdot T_s + \beta_r + \epsilon_r \quad (4)$$

209 Using Eqs. 2 and 4, Eq. 3 transforms to:

$$X = \alpha \cdot T_s + \beta + \epsilon = \sum_{r=1}^{R} (\alpha_r \cdot T_s + \beta_r + \epsilon_r)$$

210 $$= T_s \sum_{r=1}^{R} \alpha_r + \sum_{r=1}^{R} \beta_r + \sum_{r=1}^{R} \epsilon_r \quad (5)$$

211 Hence, the total CRE feedback (α) is the sum of CRE feedbacks by individual CR groups
212 (α_r).

213 Figure 3 shows the contribution to SWCRE/LWCRE feedback of each CR group and
214 reveals a distinct contrast between the two seasons. In DJF, total CRE feedback is dominated
215 by positive SWCRE feedback (less reflection of SW) in oceanic low-thick (L_tk) clouds (p-
216 value<0.06; Fig. 3a). Continental second-highest thick (H2_tk) and oceanic low-thin (L_tn)
217 clouds also show measurable contributions, but their magnitudes are about a quarter or less
218 than those of oceanic low-thick clouds. LWCRE feedbacks in DJF are mostly weak. On the
219 other hand, a more diverse mixture of clouds contributes to SWCRE/LWCRE feedbacks both
220 positively and negatively in boreal summer (Fig. 3c). For example, similarly large positive
221 SWCRE feedbacks are reported by oceanic Mid, L_tk, and L_tn clouds and continental Mid
222 clouds (all p-values<0.08) while notable negative feedbacks are contributed by tropical
223 convective clouds (H1_tk) over ocean and land, and sparse clouds (S-Clr) over ocean (but
224 with p-values slightly over 0.1). The across-group variability of LWCRE feedback in JJA is
225 similar to that of SWCRE feedback, but with opposite sign. The SWCRE (LWCRE) feedback
226 decomposition in JJA indicates less reflection of SW (more escape of LW) by various clouds,
227 while H1_tk and S-Clr clouds reflect SW (trap LW) more as surface warms.

228 The contrast between DJF and JJA seasons is intriguing and requires more in-depth
229 analysis. The following subsection shows such an analysis, specifically whether CRE
230 feedbacks are due to the changes in CR group cloud properties or due to the changes in their
231 RFO.

232

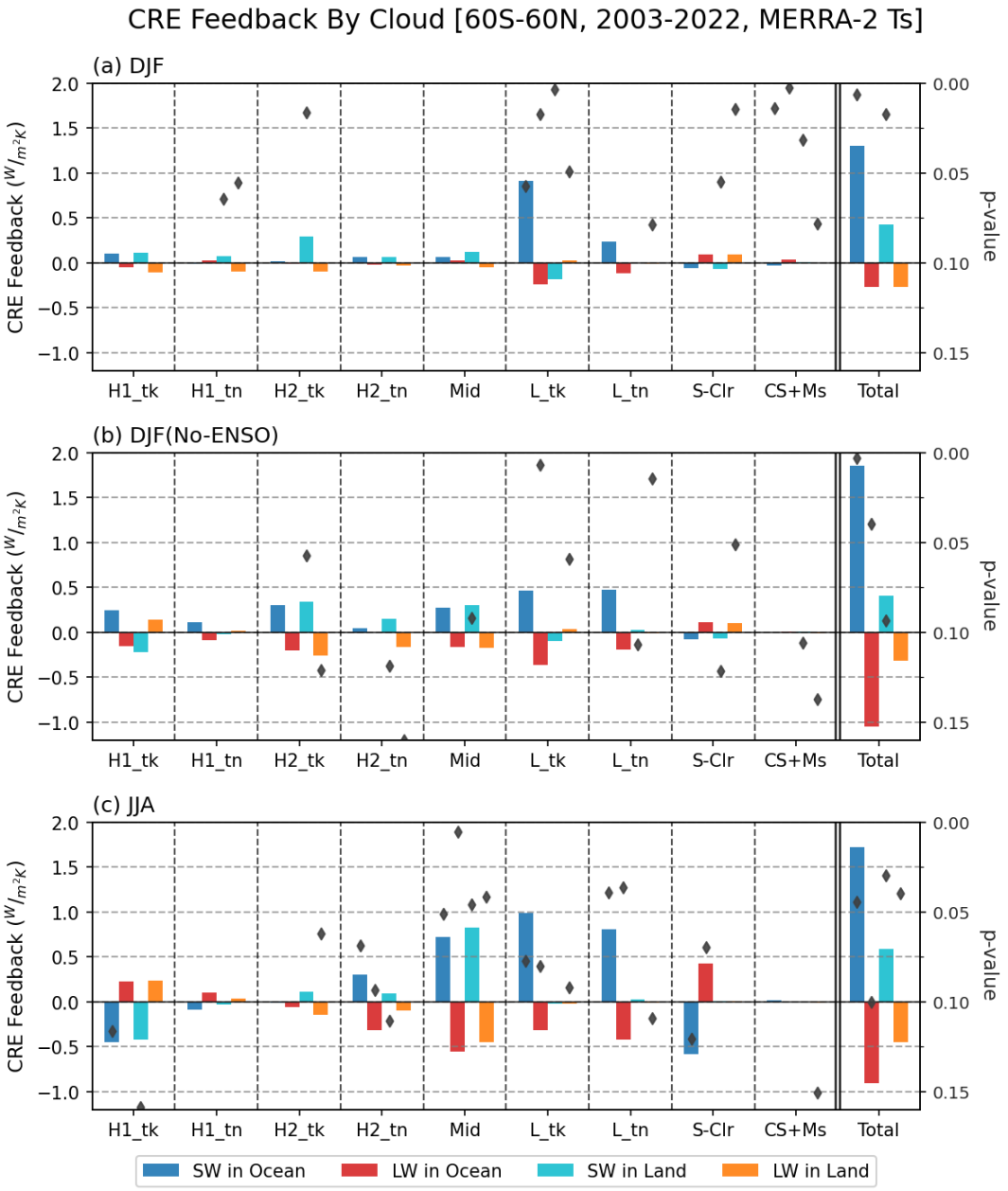

Fig. 3. Decomposition of CRE feedback by CR groups in (a) DJF, (b) No-ENSO DJF, and (c) JJA. SWCRE feedback over Ocean (dark blue) and Land (light blue), and LWCRE feedback over Ocean (red) and Land (orange). The rightmost column ("Total") shows sums of each term for all CR groups and "CS+Ms" grid cells. Diamond symbols show the corresponding regression p-value along the secondary y-axis on the right side (only if p-value is less than 0.16).

c. Further decomposition for cloud property change vs. occurrence frequency change

As shown in Z22's Eq. 2, X anomalies can be decomposed to three terms per CR group, namely due to the changes in cloud property, changes in RFO, and their covariance. When Z22's Eq. 2 is applied to our Eq. 3:

$$\Delta X = \sum_{r=1}^{R} \left(\overline{f_r} \cdot \Delta X_r + \Delta f_r \cdot \overline{X_r} + \Delta f_r \cdot \Delta X_r \right) \quad (6)$$

Equation 6 indicates that the total CRE change ΔX consists of within-group (or internal) CRE changes ΔX_r multiplied by mean RFO $\overline{f_r}$ and CR group RFO changes Δf_r multiplied by mean CRE $\overline{X_r}$; covariances (the 3rd term on the RHS) are usually small. In the context of CRE feedback, Eq. 6 can be rewritten as:

$$\frac{\partial X}{\partial T_s} = \alpha = \sum_{r=1}^{R} \alpha_r$$

$$= \sum_{r=1}^{R} \left(\bar{f_r} \cdot \frac{\partial X_r}{\partial T_s} + \frac{\partial f_r}{\partial T_s} \cdot \overline{X_r} + \frac{\partial f_r}{\partial T_s} \cdot \frac{\partial \mathrm{X}_r}{\partial T_s} \right) \quad (7)$$

where the interpretation of right-hand side is essentially same to that in Eq. 6.

An example of how Eq. 7 can be visually conveyed is provided in Fig. 4 for oceanic SWCRE feedback. Other SWCRE and LWCRE results are shown in Supplementary Figs. S3, S4 and S5. Consistent with Fig. 3a, the results in DJF (Fig. 4a) show dominant signal of L_tk clouds for oceanic SWCRE feedback, and, moreover, most of the positive feedback of these clouds comes from RFO changes (green bar; i.e., decreased occurrence of L_tk clouds with warming weighted by negative mean SWCRE). Notable signals due to the RFO changes also occur in JJA (Fig. 4c). During that season, tropical convective clouds (H1_tk) and sparse clouds (S-Clr) exhibit negative feedback while Mid and low clouds (L_tk and L_tn) exhibit positive feedback, with the RFO component being dominant with p-value<0.1 except for the L_tk clouds (more details about the CRE feedback of this group are examined in Section 4b). However, it is worth noting that while the individual within-group CRE change terms are small, they are mostly of the same sign, which results in a larger total CRE feedback than that due to RFO change terms.

Beyond these oceanic SWCRE feedbacks, we likewise generally find that the RFO-change terms $\Delta f_r \cdot \overline{X_r}$ are larger than the internal CRE-change terms for these CR groups except for L_tk (Supplementary Figs. S3, S4, and S5), although the individual RFO terms are often competing with opposite signs. For example, for the continental SWCRE feedback in JJA, the positive contribution of the Mid clouds' RFO-change term is compensated by the negative RFO-change term of tropical convective clouds (H1_tk). Again, the magnitudes of

the internal CRE-change term $\overline{f_r} \cdot \Delta X_r$ for individual CR groups are much smaller than those of the RFO-change terms, but the "no-offset" feature results in a larger total CRE feedback.

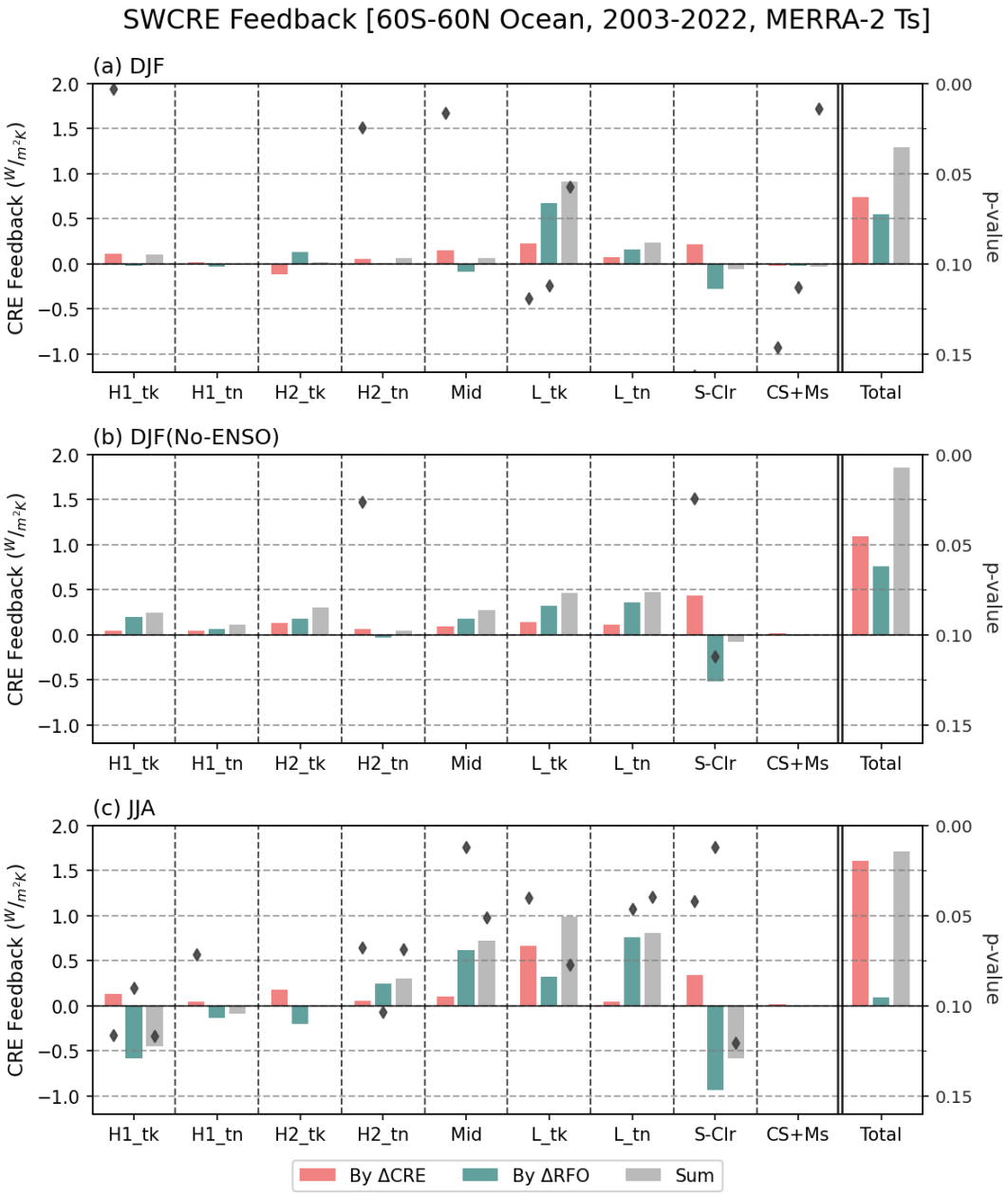

Fig. 4. Decomposition of oceanic SWCRE feedback by CR groups and by (internal) "CRE change (dark red)" and "RFO change (dark green)" terms for (a) DJF, (b) No-ENSO DJF and (c) JJA. The (typically small) covariance term in Eq. 7 is not shown here, but the gray bar is actually the sum of all three terms. As in Fig. 3, p-value is marked with the gray diamond symbol, and the right most column ("Total") shows sums of each term for all CR groups (thus p-values being unavailable for "Total" column).

To investigate further the RFO change, we applied the same linear regression against T_s, but to the DJF and JJA mean RFO maps of each CR group (Figs. 5 and 6, respectively). In DJF, tropical high clouds (H1_tk [Fig. 5a] and H1_tn [Fig. 5b]) commonly show typical ENSO responses: negative signals in the Maritime continent and positive signals in the central-to-eastern equatorial Pacific. L_tn (Fig. 5g) and S-Clr (Fig. 5h) clouds also exhibit an organized pattern with opposite signs compared to tropical high clouds, mostly consistent with Park and Leovy (2004). Over ocean, three CR groups show large domain mean RFO response to T_s: L_tk (-1.0%/K), L_tn (-0.8%/K), and S-Clr (1.6%/K). Considering that the global sum CR group RFOs should always be 1 (=100% when including CS+Ms grid cells), it appears that the increase of S-Clr clouds is compensated by the decrease of L_tk and L_tn clouds with warming. However, Fig. 4a showed that the positive feedback by the RFO-change term of L_tk clouds is much larger than the feedback due to the same term by L_tn and S-Clr clouds. This is because when the mean CRE of L_tk clouds is weighted to the RFO change (Eq. 7), it is much larger than that of the other two CR groups (Supplementary Fig. S1).

The RFO responses to T_s are much more varied in JJA. L_tn (Fig. 6g) and S-Clr (Fig. 6h) clouds show surprisingly large responses over ocean, but with opposite sign (-5.0%/K and 6.3%/K, respectively), which partially cancels out their contribution to the total CRE feedback (Fig. 4c). In Fig. 4c, the RFO-change terms of H1_tk and Mid clouds are also notable, but the RFO changes themselves of these clouds are rather smaller (0.5%/K and -1.18%/K, respectively). As is the case for L_tk clouds in DJF, the relatively large mean CREs of these CR groups explain this apparent discrepancy. Based on these RFO responses to T_s, and considering the characteristics of RFO, we hypothesize a systematic transition of clouds from one group to another has occurred as T_s rises, something we discuss in Section 4c.

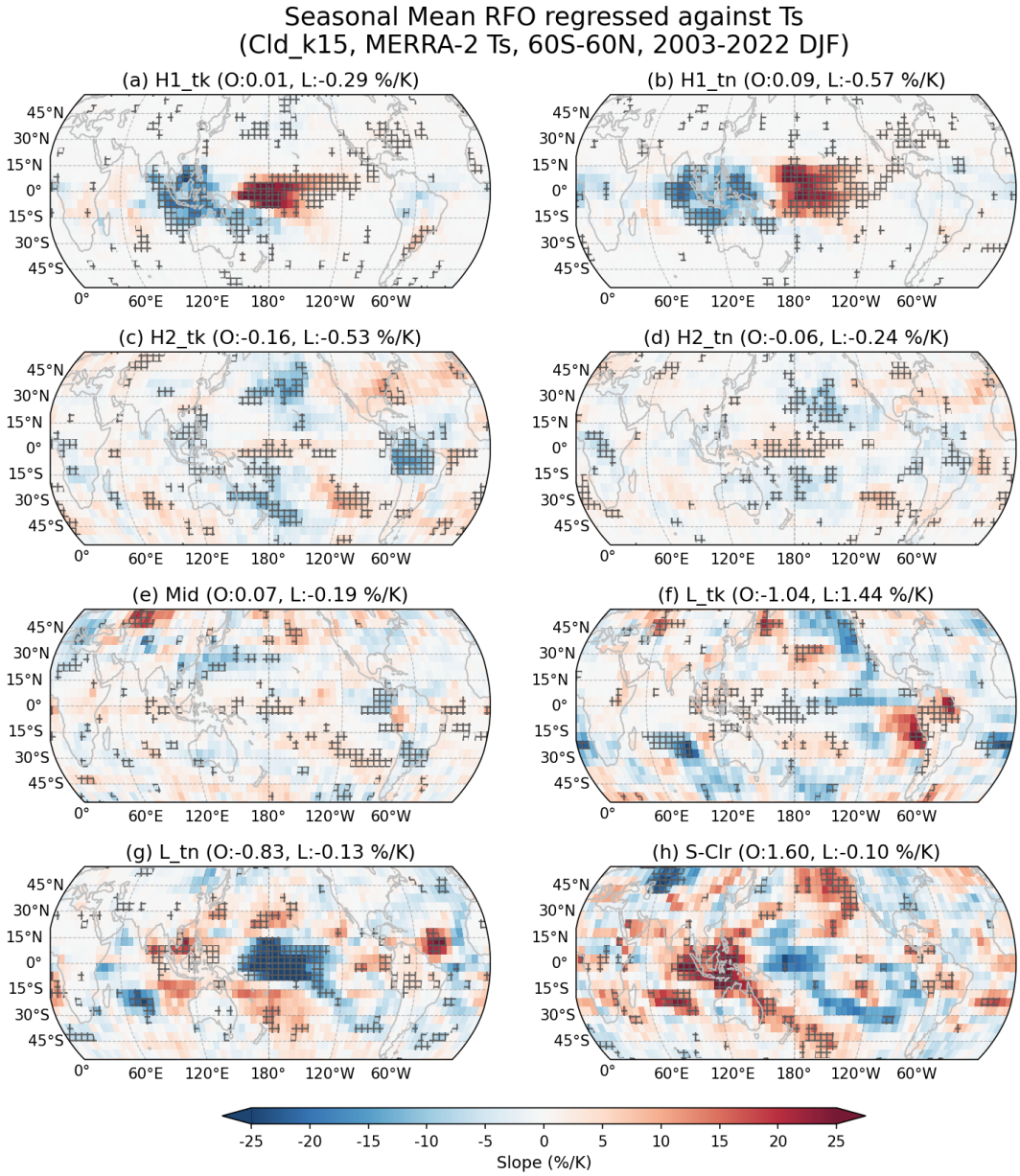

Fig. 5. Boreal winter seasonal mean RFO of each CR group regressed against T_s after degrading original 1-deg grid cell to 5-deg resolution. The weighted domain mean of regression slopes is provided above each panel, for ocean and land separately. Hatched area indicates regression p-values of smaller or equal to 0.05.

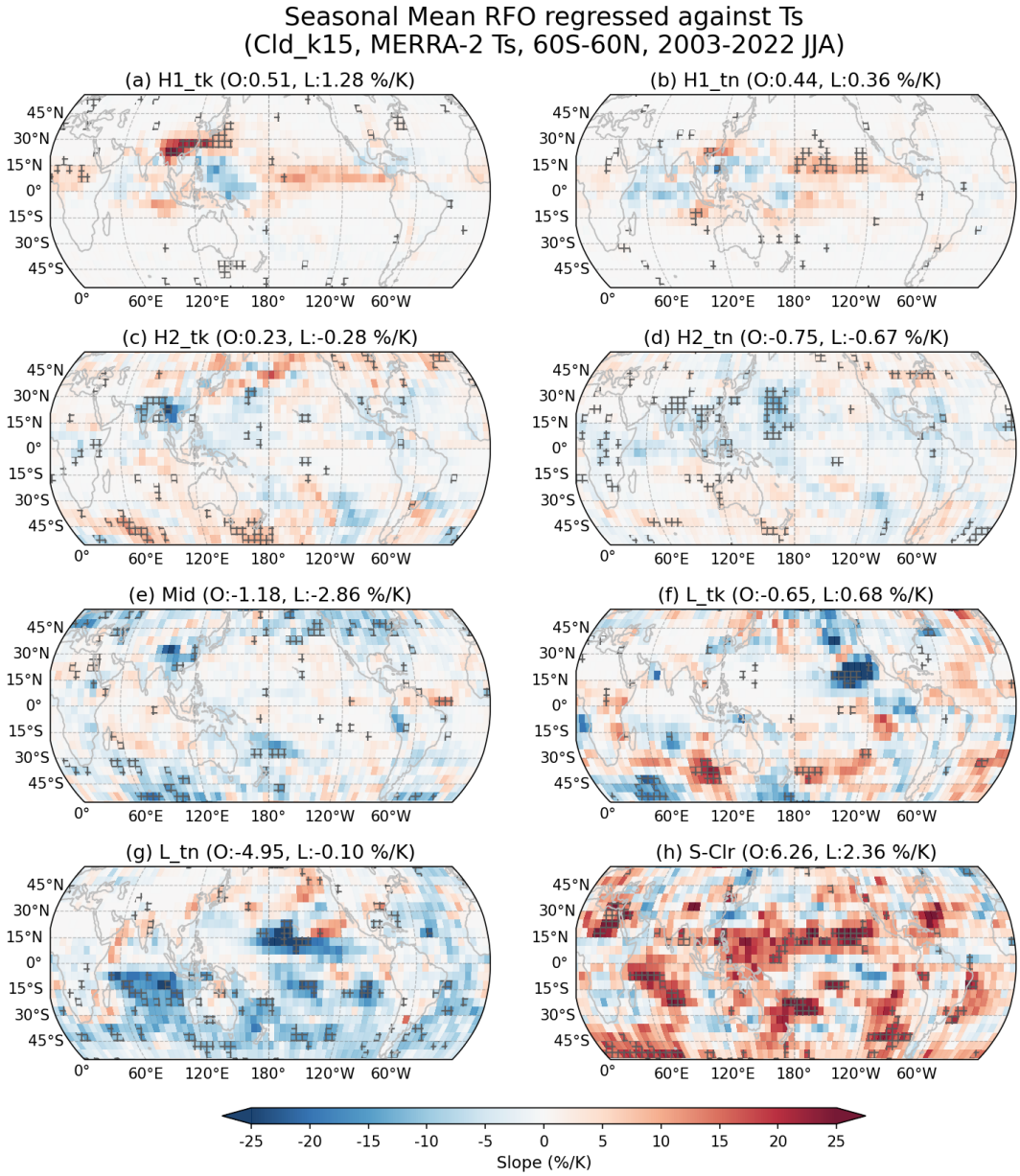

Fig. 6. As Fig. 5, but for boreal summer.

4. Discussion

a. The role of ENSO in boreal winter

Using our decomposition, we found that total CRE feedback in DJF is dominated by the positive SWCRE feedback caused by fewer oceanic L_tk clouds under warming. This result is consistent with several previous model-based studies (e.g., Koshiro et al., 2022; Zelinka et

al., 2016). However, such CRE feedback behavior is limited to DJF, which raises the possibility that seasonal characteristics strongly affect the feedback signal.

Boreal winter is known for peak ENSO activity. ENSO is a strong interannual variability affecting the globe by setting a distinctive SST pattern, which modulates notable anomalies in TOA radiation budget. This is reminiscent of the "SST pattern effect" (Stevens et al. 2016), which is the term used for describing how a spatial pattern of SST driven by global warming shapes global cloud feedback, and which has generally been studied at multidecadal time scales (e.g., Andrews et al., 2015; Zhou et al., 2016). At short time scales of less than two decades, as in this study, the ENSO-driven short-lived SST pattern can significantly affect the CRE feedback, making it comparable to the global warming signal itself (Ceppi and Fueglistaler 2021; Zhou et al. 2015). This is particularly true for our study period which includes the historically strong El Niño event of 2015-16.

We tested various aspects of the effect of ENSO on CRE feedback, and found the effects to be rather intricate. First, we tested relationships among CRE, T_s, and ENSO indices and produced figures similar to Fig. 2. Supplementary Figs. S6 and S7 show that ENSO indices and T_s correlate strongly in DJF (coefficients close to 0.7 with p-value 0.001), but this is not true when the relationships between near-global mean SWCRE/LWCRE and ENSO indices are examined (coefficient magnitudes are below 0.3 and insignificant at 90% confidence level). These two correlation analyses indicate that the direct impact of ENSO on the near-global mean CRE is relatively weak, suggesting compensating effects among various CR groups regionally. We also tested Fig. 5-like RFO response map to Niño 3.4 index (Supplementary Fig. S8) to gauge how cloud occurrences respond to ENSO. Consistent with the strong correlation between T_s and Niño 3.4 index, Supplementary Fig. S8 is essentially the same as Fig. 5. This means that an ENSO-induced SST pattern sets the boreal winter cloud occurrence pattern.

In order to examine the CRE compensations due to ENSO responses, we performed the decomposition of ENSO effect on CRE by replacing T_s in Eqs. 5, and 7 with the Niño 3.4 index, and producing figures similar to Figs. 3 and 4; i.e., we decomposed the CRE response to ENSO into contributions from RFO and internal cloud changes (Supplementary Figs. S9 and S10). These figures show that the oceanic SWCRE changes directly related to ENSO are dominated by L_tk clouds, mostly because of RFO changes (Park and Leovy 2004; Zhu et al. 2007). This contribution pattern of L_tk clouds is nearly identical to the results of Figs. 3a

and 4a, further highlighting the significant influence of ENSO on the DJF CRE feedback. We note that the dominant response of L_tk clouds to ENSO is maintained regardless of season (Supplementary Figs. S9 and S10), supporting the consistent prevalence of ENSO effects. However, JJA CRE feedback patterns shown in Figs. 3c and 4c are different from those of the ENSO-only CRE responses, probably due to the weakened ENSO in boreal summer. On the other hand, besides the individual CR group responses, the total CRE response to ENSO for all clouds shown in the right-most column is notably different between Fig. 3a and Supplementary Fig. S9a. In the case of the CRE response to ENSO, the large positive signal of L_tk clouds is compensated by other clouds, thus resulting in much smaller feedback overall, while Fig. 3 showed larger total feedback than that from the L_tk group alone. This indicates that the re-distribution of clouds by ENSO does not create large global mean CRE anomalies due to offsets, which may be related to the weaker correlation between near-global mean CRE and ENSO indices shown in Supplementary Fig. S7.

To study these issues further, we conducted an additional decomposition (namely, "No-ENSO") where the ENSO signal was removed from T_s seasonal means before recalculating the CRE feedback (i.e., using residuals after linear regression against the Niño 3.4 index). The DJF result is presented in Figs. 2b, 2e, 3b, and 4b, while JJA result is omitted since there is no qualitative difference between original and No-ENSO CRE feedbacks (i.e., the effect of ENSO in boreal summer is weak to begin with). In terms of near-global mean CRE feedback, the magnitudes of both SWCRE and LWCRE feedback are enhanced in DJF. For example, in Figs 2b and 2e, SWCRE feedback increases from 1.73 to 2.26, and LWCRE feedback also strengthens from -0.54 to -1.37, when the ENSO signal is excluded. In the case of LWCRE, the correlation becomes much stronger (-0.27 to -0.52), and the p-value decreases below 0.1. The contribution pattern by CR groups also dramatically changes (Fig. 3b); the dominant role in oceanic SWCRE feedback of L_tk clouds disappears and various CR groups contribute equitably to the total cloud feedback, particularly for both oceanic SWCRE and LWCRE (e.g., H1_tk, H2_tk, Mid, and L_tn). In addition, these oceanic feedback signals are mostly accompanied by high p-values indicating increased uncertainty. The decomposition figure (Fig. 4b) shows that the magnitudes of RFO-change terms are generally larger than those of CRE-change terms, but also come with high p-values, warranting future study with longer time series.

One interesting point here is that the RFO contribution to oceanic SWCRE feedbacks is positive for most CR groups except S-Clr clouds (Fig. 4b). Considering the relatively weak mean SWCRE of S-Clr clouds, a significant increase of S-Clr RFO is expected globally. We produced the same figure of RFO trend map as Fig. 5, but with No-ENSO T_s, and found that the RFO of S-Clr clouds increases at the rate of 2.91%/K over ocean (Fig. 7h). This indicates that global warming may suppress the occurrence of thicker or higher clouds, but lead to an increase of cloud-sparse scenes in boreal winter ocean, if the effect of ENSO weakens, although the statistical significance of RFO change with No-ENSO T_s is rather weak. Overall, the global distributions of positive and negative RFO signals of CR groups in the no-ENSO regression of Fig. 7 seem far noisier that those in Figs. 5 and 6. Lastly, it is worth noting that, in Fig. 4b, oceanic SWCRE contribution of S-Clr clouds is actually small because the large negative RFO-change term is compensated by the positive internal CRE-change term, which means that S-Clr clouds become thinner or of smaller cloud fraction (CF) with higher T_s. This internally changing feature of S-Clr clouds is also noticeable in JJA (both p-values are less than 0.05), and its details are examined in the next subsection.

Returning to L_tk clouds, our results can be interpreted as showing that the higher T_s in El Niño conditions coincide with fewer oceanic low-thick clouds, which results in more absorption of SW radiation. The regions of notable negative RFO trend of L_tk clouds include the equatorial eastern Pacific, northeastern Pacific, southeastern Indian Ocean, and southeastern Atlantic Ocean (Fig. 5f). Among them, it is interesting that, when RFO is regressed against No-ENSO T_s, the signals flip in the equatorial eastern Pacific and southeastern Indian Ocean while the signal in the southeastern Atlantic Ocean remains consistently negative (Fig. 7f). The details of these regional differences merit further examination in future studies. In addition, the northeastern Pacific also deserves special attention. The negative RFO signal of L_tk clouds implies warmer SST in this area. Actually, a notable event colloquially named “the Blob” occurred in 2013-15 (Bond et al. 2015; Di Lorenzo and Mantua 2016). This event was characterized by abnormally positive SST anomalies persisting for multiple years, and then ultimately interacting with the strong 2015-16 El Niño (Santoso et al. 2017; Tseng et al. 2017). In a relatively short (20 years) study period like ours, such a notable regional event can distort the global mean CRE feedback, but currently we cannot be sure whether “the Blob” was a random abnormal event or a global warming signal.

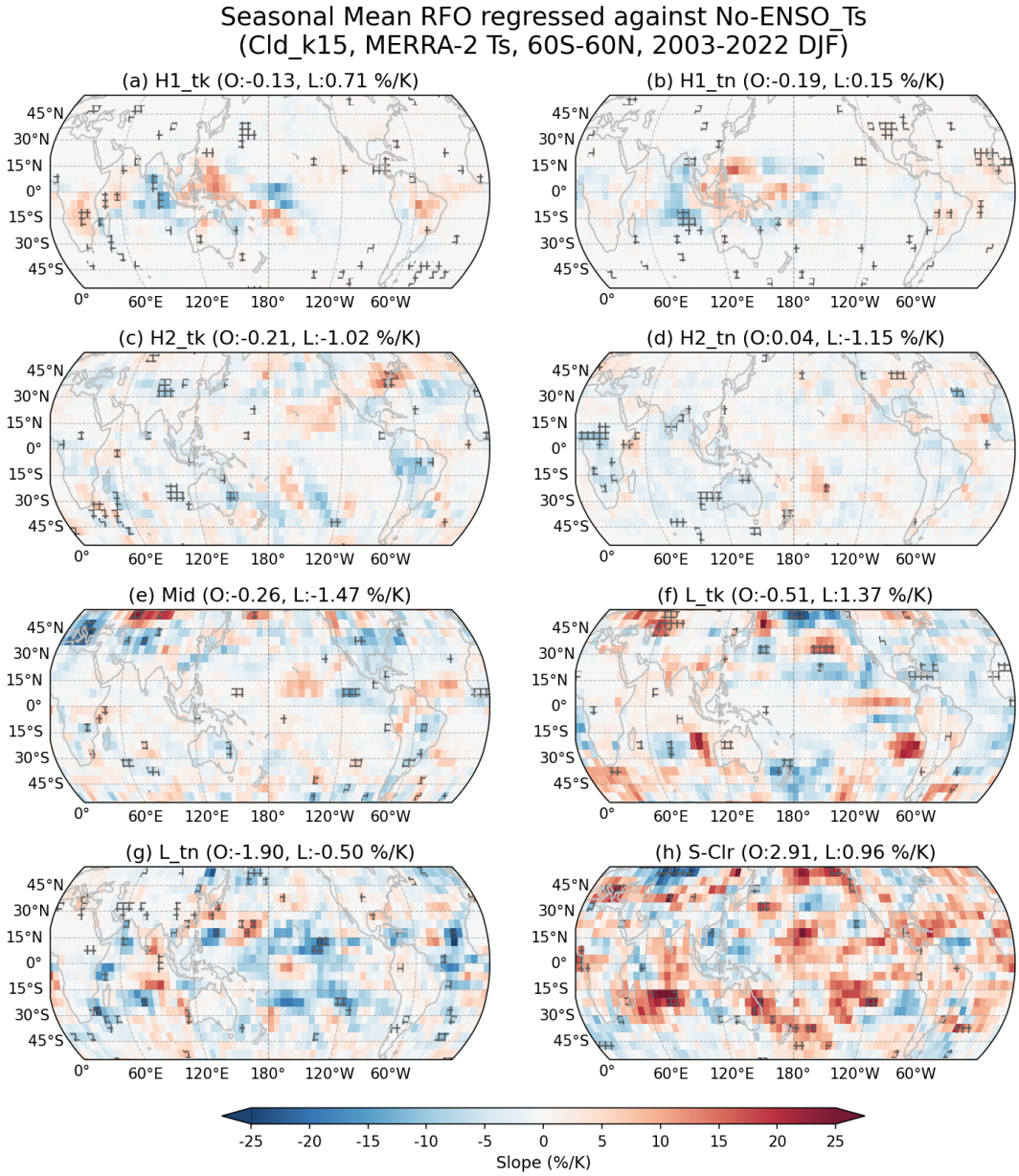

Fig. 7. As Fig. 5, but with RFO regressed against No-ENSO T_s, where the regression line of T_s against Niño 3.4 index is subtracted.

Lastly, we also tested the relationship between the Pacific Decadal Oscillation (PDO; Mantua et al., 1997) and T_s since Loeb et al. (2021) suggested a possible link between PDO and decadal changes in the Earth's energy budget. However, we found the relationship between PDO and T_s to be much weaker than that with ENSO (Supplementary Figs. S6 and S7) echoing recent work by Raghuraman et al. (2023) who found a weak relationship between PDO and CRE on a global-mean scale.

b. Internal cloud changes within CR groups

In the previous section, we found statistically significant signals of internal CRE-change term in SWCRE feedback for oceanic L_tk in JJA and S-Clr clouds in both JJA and No-ENSO DJF. To investigate this, we performed a regression against T_s of the binned CFs of the JJA seasonal mean CR group joint histograms (Fig. 8; DJF counterparts with T_s and No-ENSO T_s are shown in Supplementary Figs. S11 and S12, respectively). We performed such an analysis because CR group-mean CRE changes should be related to changes in the clouds' mean joint histogram (Zelinka et al., 2012a, 2012b, 2016, 2022). As expected, the decrease of SW reflection for L_tk and S-Clr clouds with warming appears to be due to the decrease of their CF (-2.81%/K, -1.64%/K, respectively). Moreover, regression slopes of individual binned CFs indicate that L_tk clouds become optically thinner on average (increasing in thinner bins while decreasing in thicker bins in Fig. 8f), which amplifies the reduction of SW reflection. When examining regression slopes of binned CFs for individual regimes in the L_tk group (Figs. 8i to 8l), we found that the thinning trend is more notable in CR10 and CR11, while the reduction in total CF is stronger in CR12 and CR13. The thinning trends of CR10 and CR11 are also noticeable in DJF oceans, but decreasing CF trends are much weaker, with both T_s and No-ENSO T_s (Supplementary Figs. S11 and S12), thus the smaller feedback contribution of the internal CRE-change term with weaker significance in Figs. 4a and 4b. In the case of S-Clr clouds, mean SWCRE itself is relatively small, hence the change of CF at 1-2%/K does not result in a notable change of SWCRE. However, the overwhelming RFO of S-Clr clouds amplifies the effect of even a small within-group SWCRE change.

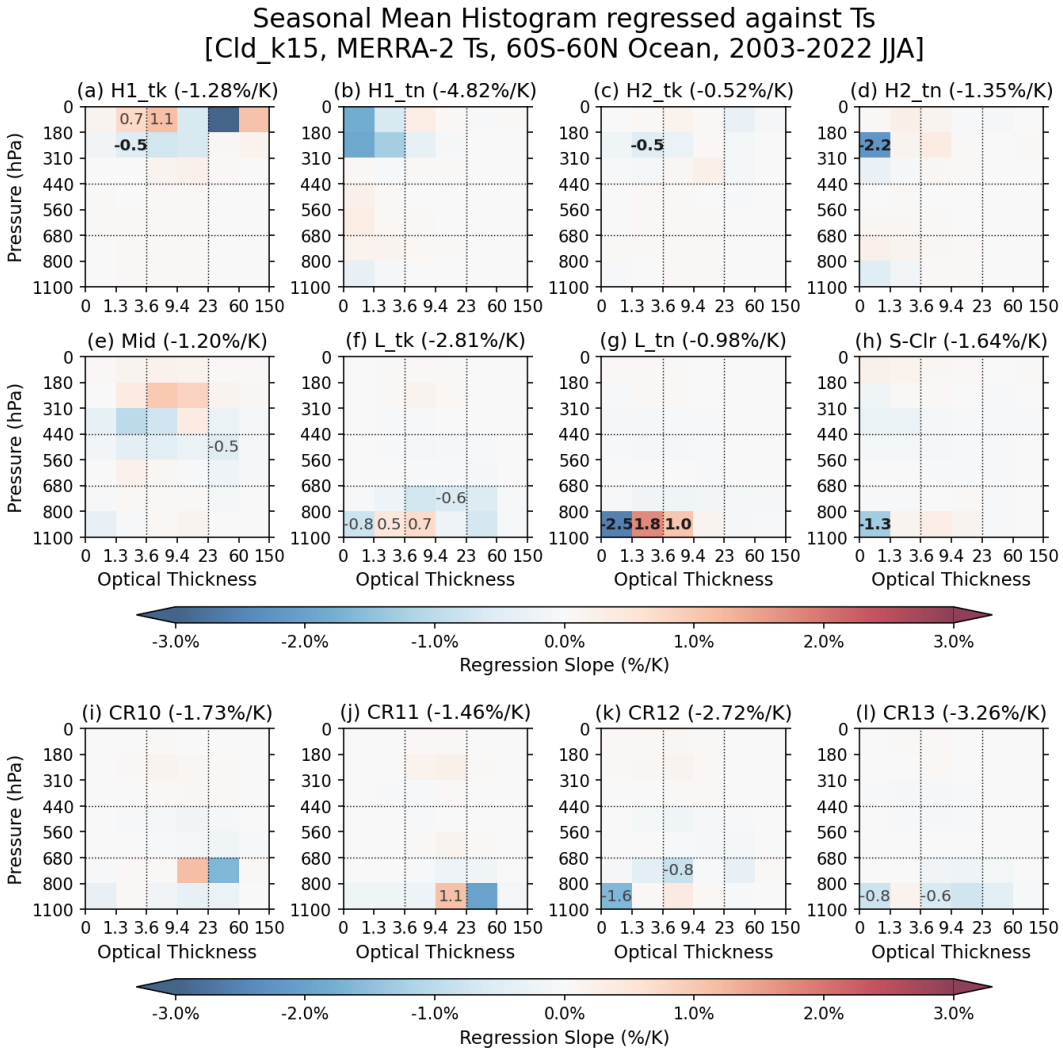

Fig. 8. Slopes of oceanic boreal summer seasonal mean joint histogram binned CFs of each CR group when regressed against T_s. Bottom four panels show the same slopes of binned CFs, but for individual CRs of the L_tk group. The sum of binned CF regression slopes is given above each panel. Slopes larger than 0.5 are explicitly shown when the corresponding p-value is below 0.1 (and in bold when the p-value is below 0.05).

On the other hand, L_tn cloud also shows overall negative regression slope of binned CF (-0.98%/K), but individual binned CF slopes show a thickening trend with a transition from the thinnest bin to the thicker bins (Fig. 8g). Hence, the near-zero feedback by CRE-change term of L_tn clouds in Fig. 4c can be interpreted as an offset between decreasing CF and thickening clouds. In addition, notable negative slopes in Cirrus clouds are detected in H1_tn and H2_tn clouds (Figs. 8b and 8d). However, the decomposition of LWCRE feedback over ocean shows the absolute magnitudes of the internal CRE-change term in H1_tn and H2_tn clouds to be quite small (CRE-change term in H1_tn clouds is of very small p-value, though; Supplementary Fig. S4c). This is partially because of weighting by the relatively small mean

RFOs of the H1_tn and H2_tn groups (about 3% and 4%, respectively; Table 1).When we tested the same regression analysis on cloud histograms of all grid cells (i.e. all CRs combined; Supplementary Figs. S13 against T_s and S14 against No-ENSO T_s), the regression slope patterns were similar to that of S-Clr (Fig. 8h) regardless of season, due to the dominant RFO of the S-Clr group, while regression slopes in other bins were near zero.

c. Hemispherical contrast and regional characteristics

In addition to the asymmetric seasonal strength of ENSO, the combination of seasonally changing insolation and uneven distribution of land and ocean can contribute to the hemispherical differences of CRE feedback. To examine this issue, we produced the Fig. 3-like plot of CRE feedback decomposition, but for the northern hemisphere (NH) and southern hemisphere (SH) separately for each season (Supplementary Fig. S15). We note that the same near-global mean T_s is used in Fig. S15 as in Figs. 3a and 3c, and No-ENSO T_s version is presented in Supplementary Fig. S16.

In boreal winter (Figs. S15a and S15d), the positive CRE feedback by oceanic L_tk clouds is commonly seen in both hemispheres, but with larger magnitude in the SH. The larger CRE due to larger insolation in summer hemisphere and larger mean RFO of L_tk clouds in the SH may contribute to this result. One interesting point is that the CRE feedback signals by H2_tk and Mid clouds in DJF cancel out between the NH and SH. For example, positive SWCRE feedback by oceanic H2_tk and Mid clouds in the NH (winter hemisphere) is being offset by negative feedback in the SH (summer hemisphere). The opposite signs of feedback signals are mostly related to the RFO-change term (not shown), yielding thus overall small feedback in Fig. 4a. In the decomposition based on No-ENSO T_s, oceanic SWCRE and LWCRE feedback signals of these two cloud groups in the SH flip over to positive, while those in the NH remain same, reflecting the hemispherically asymmetric effect of ENSO (e.g., Jin & Kirtman, 2009).

The boreal summer season also shows hemispherical differences. First, notable SWCRE feedbacks over land are seen in the NH (H1_Tk and Mid clouds) but not in the SH. In the SH, oceanic Mid, L_tn and S-Clr clouds contribute most of CRE feedbacks, which is different form the NH where L_tk and H1_tk clouds exhibit sizable signals. The comparisons between

hemispheres for their common local season (e.g., NH in DJF vs. SH in JJA or vice versa) also show dramatically different CRE feedback patterns.

These regional differences and the fact that most CRE feedbacks are due to the RFO change motivated us to examine regionally detailed RFO trends of CR groups. Hence, we derived regression slopes of JJA zonal mean RFOs against T_s for every 15° in latitudes (Fig. 9), representing the Tropics (0°-15°), Subtropics (15°-30°), Mid-latitudes (30°-45°), and High-latitudes (45°-60°) of each hemisphere. The DJF counterpart is presented in Supplementary Figs. S17 (against T_s) and S18 (against No-ENSO T_s).

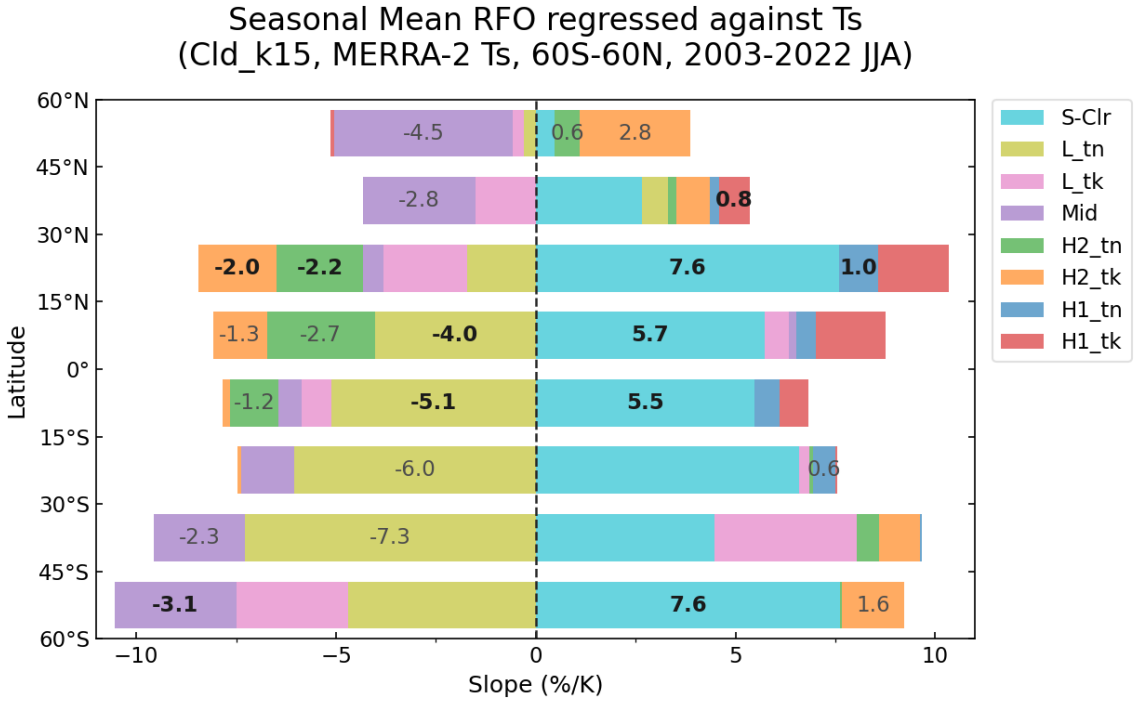

Fig. 9. Boreal summer (JJA) seasonal mean RFO of each CR group regressed against T_s after degrading to zonal means for every 15° in latitudes. CR groups of positive (right side) and negative (left side) slopes are separated and stacked on each side. The individual slope value is explicitly written when the p-value of regression is equal or below 0.1 (Bold weight if p-value ≤ 0.05).

Consistent with Fig. 6, Fig. 9 shows offsets of RFO trends between L_tn and S-Clr clouds in large areas including whole SH and northern tropics where ocean coverage dominates land. This potentially indicates that oceanic cumulus experiences decreasing CF in boreal summer as T_s increases (Fig. 8g) and some of them transition to S-Clr clouds, which needs to be examined in a future study. A similar pattern is also seen in the boreal winter season with No-

519 ENSO T_s, but with smaller magnitudes. In addition, the high cloud signals look also
520 interesting. For example, in Mid- and High-latitudes in both hemispheres, Mid clouds
521 (purple) decrease with warming, while H2_tk clouds (orange) increase. In the northern Mid-
522 latitudes, even H1_tk clouds increase in a statistically significant way. Similar transitions to
523 CR groups of higher clouds are also seen in tropics and northern subtropics where H2_tk
524 (orange) and H2_tn (green) clouds decrease while H1_tn (blue) and H1_tk (red) clouds
525 increase with warming. This is consistent with previous studies of the expansion of Hadley
526 Cell (Hu and Fu 2007; Lu et al. 2007), increasing height of tropopause in the NH (Meng et al.
527 2021), poleward migration of storm tracks and maximum intensity tropical cyclones
528 (Knutson et al. 2019; Norris et al. 2016), and rising altitudes of tropical high clouds
529 (Hartmann and Larson 2002; Richardson et al. 2022) or high clouds in all locations (Zelinka
530 et al. 2013; Norris et al. 2016). Based on the mean CRE characteristics shown in
531 Supplementary Fig. S1, both transitions of Mid to H2_tk and H2_tk to H1_tk clouds can
532 contribute to more negative SWCRE and more positive LWCRE feedbacks.

533 For the tropical deep convection (H1_tk) clouds, the northern Subtropical increasing trend
534 in Fig. 9 appears to be related to the strong positive slopes seen in southern East Asia (Fig.
535 6a). This region experienced frequent severe floods in recent years, and further studies are
536 warranted to examine if this is caused by global warming or was an isolated event. In
537 addition, the general pattern of H1_tk clouds in Fig. 6a indicates a strengthening of the
538 Intertropical Convergence Zone (ITCZ) in central to eastern equatorial Pacific (consistent to
539 Byrne et al., 2018) while decreasing convective activity in the western tropical Pacific. This
540 pattern may have also been affected by the strong 2015/16 El Niño since a warm SST
541 anomaly in the central Pacific already appeared in 2015 JJA (Capotondi et al. 2022; Santoso
542 et al. 2017).

543 Lastly, the JJA season also experienced warmer SST due to marine heatwaves along the
544 western coast of North America, namely “the Blob 2.0” in 2019 JJA (Amaya et al. 2020). In
545 Fig. 6f, the strong negative slope of L_tk RFO is also notable in this region, which partially
546 contributes to the decreasing RFO of L_tk group (pink) in the northern subtropics (Fig. 9). If
547 these marine heatwaves are exceptional cases, the negative slope of L_tk RFO would
548 moderate with a longer timeseries, making the positive SWCRE feedback weaker.

549

550 ## 5. Summary and conclusions

Twenty years of satellite data of cloud and radiation allowed us to examine the details of observed CRE feedback. By employing the decomposition method to distinguish the contributions due to internal CRE changes and RFO changes of individual cloud regime (CR) groups, we were able to gain insight on the seasonal characteristics of CRE feedback even with a limited number of samples.

We found that SWCRE feedback by oceanic low-thick (L_tk) clouds dominates global CRE feedback during DJF, and particularly the decreasing RFO of L_tk clouds with surface warming yields positive SWCRE feedback. We also accounted for the effect of ENSO on this CRE feedback since ENSO sets up a unique spatial distribution pattern of SST which perhaps can be used as a proxy for the so-called "pattern effect" on CRE feedback. When doing so, the dominance of SWCRE feedback by L_tk clouds seemed to most likely originate from ENSO. ENSO also disturbs LWCRE feedback by reducing its magnitude, and results in weaker correlation between LWCRE and T_s.

During the JJA season, we found notable signals in the within-group CRE change term for oceanic L_tk and sparse (S-Clr) clouds. Further regression analysis of cloud fraction distributions against T_s showed that both the thinning of clouds and the decrease of overall CF within CR groups can explain the internal CRE-change signal. Another characteristic of JJA feedback is that various CR groups have competing positive and negative global CRE feedbacks. For example, mid and low clouds contribute to a positive SWCRE feedback while tropical convective (H1_tk) clouds and S-Clr clouds offset it. These effects are mostly due to the decreasing and increasing RFO of corresponding CR groups with warmer T_s except the aforementioned oceanic L_tk and S-Clr clouds. From additional analysis of RFO change by T_s, the following two signals were found as the global warming responses:

1) Decreasing occurrence of cumulus resulting in larger clear-sky fractions, particularly over oceans.

2) Transition to higher top convective clouds in most regions except southern subtropics.

The second finding is mostly exclusive to boreal summer, while the decreasing L_tn and increasing S-Clr clouds are also seen in DJF with weaker magnitude.

The stronger effect of ENSO during DJF than JJA is an obvious reason for the dramatic contrast between the two seasons. When we examined the CRE feedback components with ENSO-excluded T_s, we found that the magnitudes of total CRE feedbacks are similar between

DJF and JJA (Fig. 3b vs. 3c). However, notable differences of CRE feedbacks between the two seasons remain if we examine details by CR group. Hence this study suggests that seasonal separation is advisable for more accurate feedback assessment. This is particularly true because it is uncertain whether ENSO's effect on CRE feedback is linear: if it is not, a model-based long-term average will not cancel out the effects of ENSO's opposite phases on CRE feedback. Considering a recent study of Williams et al. (2023) which suggests non-linear responses of climate to tropical SSTs, a sophisticated feedback assessment accounting for ENSO effects would be warranted.

Acknowledgments.

Resources supporting this work were provided by the NASA High-End Computing (HEC) Program through the NASA Center for Climate Simulation (NCCS) at Goddard Space Flight Center. LO acknowledges support by NASA's MEaSUREs program. RK is supported by NASA's Science of Terra, Aqua and Suomi-NPP program (grant no. 80NSSC21K1968) and CloudSat/CALIPSO Science program (grant no. 80NSSC23K0207).

Data Availability Statement.

The cloud-only regime dataset defined in 50ºN-50ºS (but assigned to 60ºN-60ºS domain; including centroids, CR-number-on-map, and sample code to calculate regime mean CRE) is available at https://data.nasa.gov/Earth-Science/Cloud-Regime-for-CRE-Feedback-Study/g6w2-43cq. Surface temperature data of MERRA-2 (tavg1_2d_slv_Nx, doi: 10.5067/VJAFPLI1CSIV) were obtained from Goddard Earth Sciences Data and Information Services Center (GES DISC; https://disc.gsfc.nasa.gov/), Greenbelt, MD, USA. The Level-3 (L3) MODIS Atmosphere Daily Global Product of Terra (MOD08_D3, doi: 10.5067/MODIS/MOD08_D3.061) and Aqua (MYD08_D3, doi: 10.5067/MODIS/MYD08_D3.061) was obtained from the Level-1 and Atmosphere Archive & Distribution System (LAADS) Distributed Active Archive Center (DAAC; https://ladsweb.modaps.eosdis.nasa.gov/) in the Goddard Space Flight Center, Greenbelt, MD, USA. CERES FluxByCldType – Level 3 (doi: 10.5067/Terra-Aqua/CERES/FLUXBYCLDTYP-DAY_L3.004A) and EBAF-TOA -Level 3b (doi:

10.5067/TERRA-AQUA/CERES/EBAF-TOA_L3B004.1) was obtained from the NASA Langley Research Center CERES ordering tool at https://ceres.larc.nasa.gov/data/.

APPENDIX

Details of Cloud Regimes

The cloud regimes (CRs) were derived from *k*-means clustering of ISCCP-like 2D joint histograms of MODIS COT and CTP (Collection 6.1; Platnick et al., 2017, 2018), both Terra and Aqua joint histograms in the 50°S-50°N domain from June 2014 to May 2019. Jin et al. 2021 presented detailed steps to obtain CRs like data preparation, initialization for clustering, and objective criteria for selecting optimal number of clusters (k=15 in this case).

The original 15 CRs are composed of 9 high-cloud CRs, 5 low-cloud CRs, and the semi-clear CR15 which includes various broken clouds of low cloud fraction (CF). A second round of clustering was applied only to the histograms assigned to CR15 and produced three sub-CRs (15A, 15B, and 15C). The major sub-regime of these in terms of RFO is still a low-CF CR (semi-clear; CR15C), while the other two sub-CRs appear to be dominated by mid-level cloud. These total 17 CRs (including sub-regimes) are displayed in Appendix Fig. A1, where the CRs are organized into CR groups.

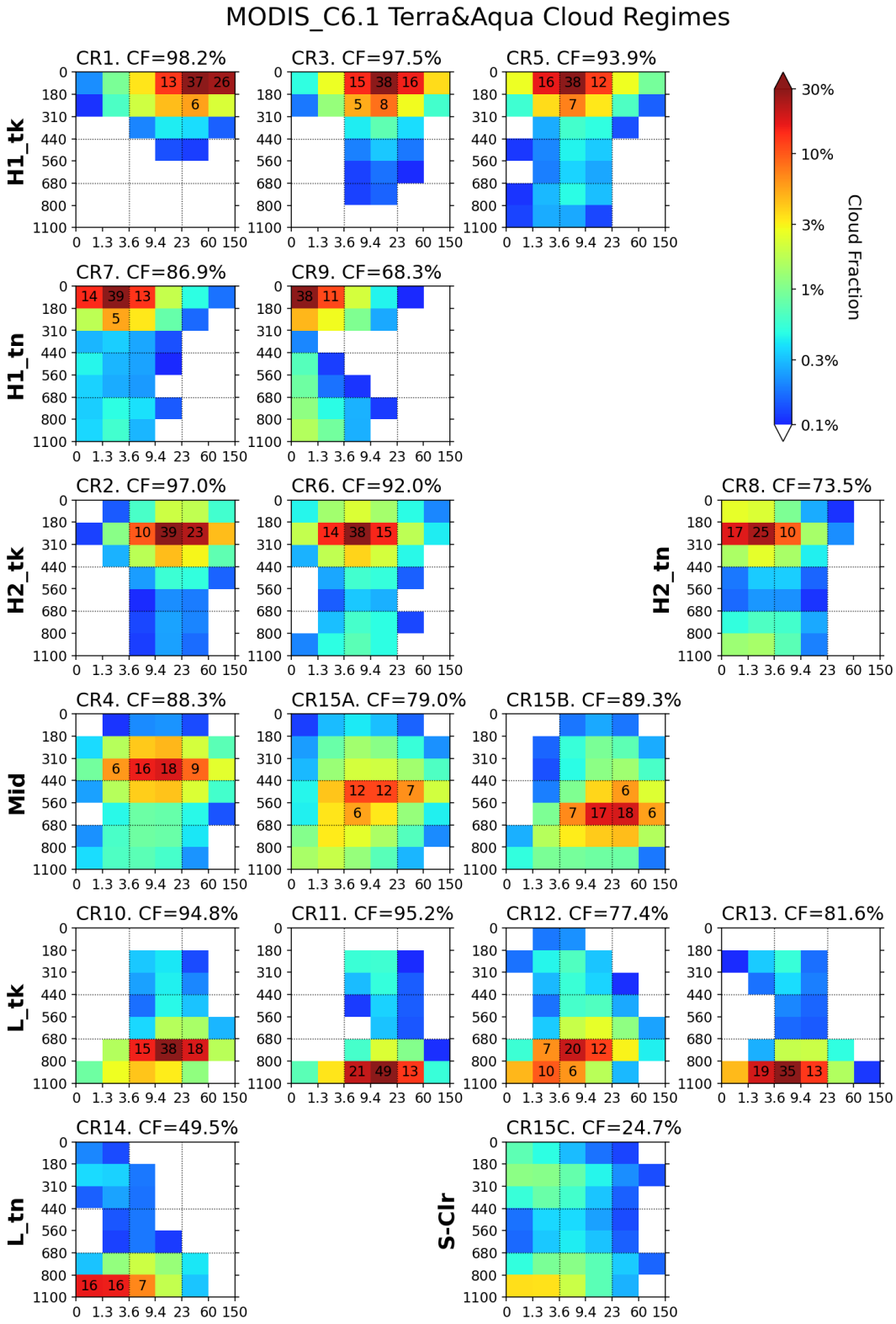

630

631 Fig. A1. Cloud regime (CR) centroid (mean histograms) that is organized into CR groups.
632 Bin CF values exceeding 5% are shown explicitly on the centroid panels. The total CF of
633 each CR is provided above each panel.

634

While the clustering process used distinct Terra and Aqua joint histograms (at daily 1° resolution), regime assignment for a particular grid cell was performed using the average Terra-Aqua joint histogram (TA_mean). This approach minimizes unassigned grid cells and ensures that the cloud classification represents daytime mean observations. Appendix Fig. A2 show the geographical distribution of relative frequency of occurrence (RFO) of total 17 CRs including three sub-regimes of the CR15, where domain and period are set to same as those in Jin et al. (2021).

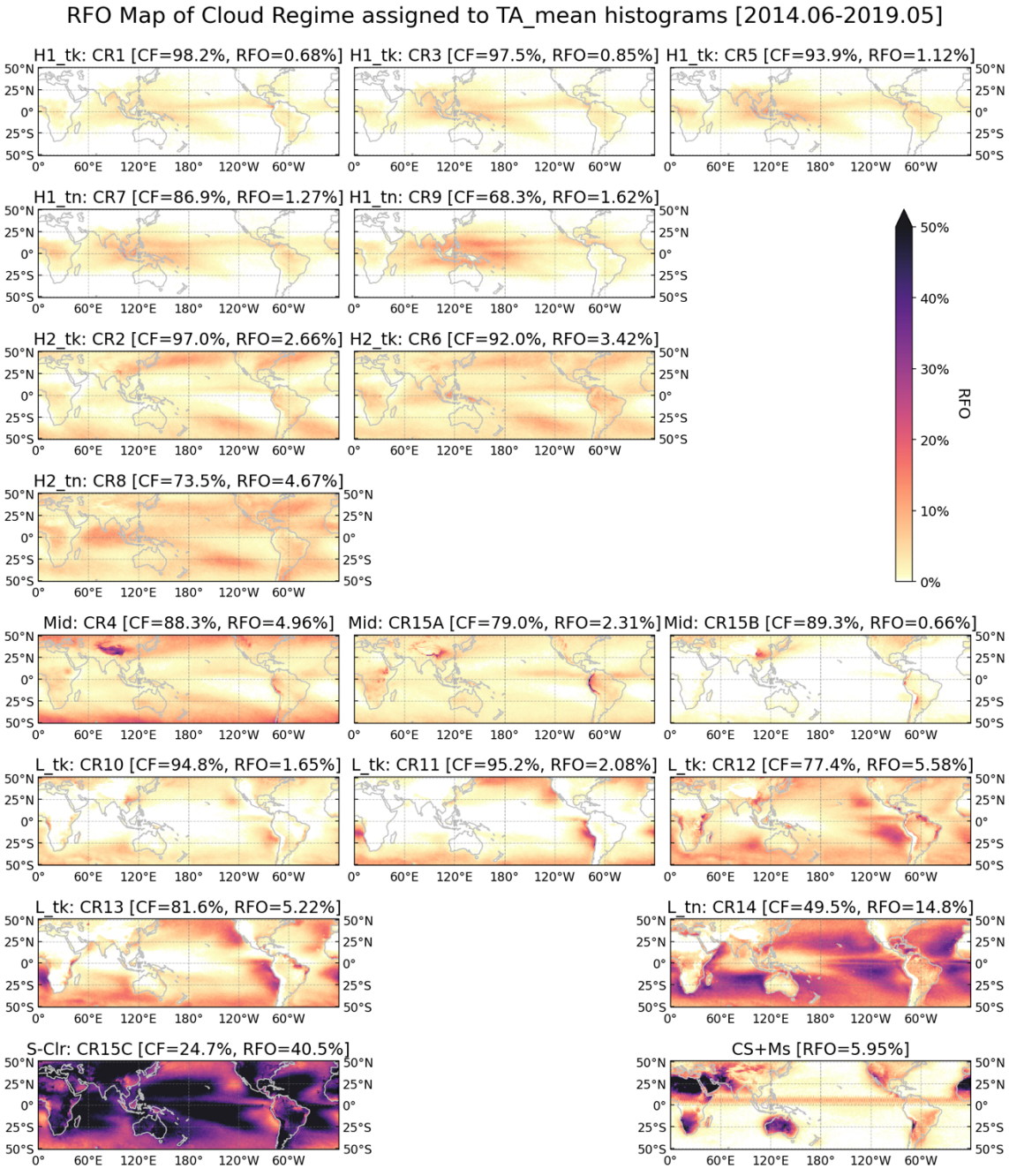

Fig. A2. Geographical distribution of relative frequency of occurrence (RFO) of each CR after Terra-Aqua grid cell mean histograms were assigned, and which are also re-arranged as Fig. A1. CR mean RFOs are provided above the map panels.

The geographical distributions of RFOs in Appendix Fig. A2 are almost identical to the original RFO distributions shown in Supplementary Fig. SB5 in Jin et al. (2021). However, the nature of TA_mean histograms caused the change in mean RFO values. First, most mean RFO values increase with TA_mean histograms because the fraction of missing grid cells decreases from about 10% to 5%, which translates to a relative 5.6% increase for each CR. However, the increase of semi-clear CR15 mean RFO (31.6% to 43.5%; a 37.6% relative increase) is far exceeding the level that can be explained by the decreasing missing data effect. This means that weather transitions from local morning to afternoon dilutes cloud activity that would otherwise be classified as one of the other CRs.

REFERENCES

Afyouni, S., S. M. Smith, and T. E. Nichols, 2019: Effective degrees of freedom of the Pearson's correlation coefficient under autocorrelation. *NeuroImage*, **199**, 609–625, https://doi.org/10.1016/j.neuroimage.2019.05.011.

Amaya, D. J., A. J. Miller, S.-P. Xie, and Y. Kosaka, 2020: Physical drivers of the summer 2019 North Pacific marine heatwave. *Nat Commun*, **11**, 1903, https://doi.org/10.1038/s41467-020-15820-w.

Andrews, T., J. M. Gregory, and M. J. Webb, 2015: The Dependence of Radiative Forcing and Feedback on Evolving Patterns of Surface Temperature Change in Climate Models. *J. Climate*, **28**, 1630–1648, https://doi.org/10.1175/JCLI-D-14-00545.1.

Bodas-Salcedo, A., and Coauthors, 2011: COSP: Satellite simulation software for model assessment. *Bull. Am. Meteorol. Soc.*, **92**, 1023–1043, https://doi.org/10.1175/2011BAMS2856.1.

Bond, N. A., M. F. Cronin, H. Freeland, and N. Mantua, 2015: Causes and impacts of the 2014 warm anomaly in the NE Pacific. *Geophys. Res. Lett.*, **42**, 3414–3420, https://doi.org/10.1002/2015GL063306.

Bony, S., A. Semie, R. J. Kramer, B. Soden, A. M. Tompkins, and K. A. Emanuel, 2020: Observed Modulation of the Tropical Radiation Budget by Deep Convective Organization and Lower-Tropospheric Stability. *AGU Advances*, **1**, e2019AV000155, https://doi.org/10.1029/2019AV000155.

679 Byrne, M. P., A. G. Pendergrass, A. D. Rapp, and K. R. Wodzicki, 2018: Response of the
680 Intertropical Convergence Zone to Climate Change: Location, Width, and Strength.
681 *Curr Clim Change Rep*, **4**, 355–370, https://doi.org/10.1007/s40641-018-0110-5.

682 Capotondi, A., M. Newman, T. Xu, and E. Di Lorenzo, 2022: An Optimal Precursor of
683 Northeast Pacific Marine Heatwaves and Central Pacific El Niño Events. *Geophysical*
684 *Research Letters*, **49**, https://doi.org/10.1029/2021GL097350.

685 Ceppi, P., and S. Fueglistaler, 2021: The El Niño–Southern Oscillation Pattern Effect.
686 *Geophysical Research Letters*, **48**, e2021GL095261,
687 https://doi.org/10.1029/2021GL095261.

688 Cess, R. D., and Coauthors, 1990: Intercomparison and interpretation of climate feedback
689 processes in 19 atmospheric general circulation models. *J. Geophys. Res.*, **95**, 16601–
690 16615, https://doi.org/10.1029/JD095iD10p16601.

691 ——, and Coauthors, 1996: Cloud feedback in atmospheric general circulation models: An
692 update. *J. Geophys. Res.*, **101**, 12791–12794, https://doi.org/10.1029/96JD00822.

693 Chung, E.-S., and B. J. Soden, 2018: On the compensation between cloud feedback and cloud
694 adjustment in climate models. *Climate Dynamics*, **50**, 1267–1276,
695 https://doi.org/10.1007/s00382-017-3682-1.

696 Colman, R., 2003: A comparison of climate feedbacks in general circulation models. *Climate*
697 *Dynamics*, **20**, 865–873, https://doi.org/10.1007/s00382-003-0310-z.

698 Colman, R. A., and B. J. McAvaney, 1997: A study of general circulation model climate
699 feedbacks determined from perturbed sea surface temperature experiments. *J.*
700 *Geophys. Res.*, **102**, 19383–19402, https://doi.org/10.1029/97JD00206.

701 Di Lorenzo, E., and N. Mantua, 2016: Multi-year persistence of the 2014/15 North Pacific
702 marine heatwave. *Nature Clim Change*, **6**, 1042–1047,
703 https://doi.org/10.1038/nclimate3082.

704 Forster, P., and Coauthors, 2021: The Earth's Energy Budget, Climate Feedbacks, and
705 Climate Sensitivity. *Climate Change 2021: The Physical Science Basis. Contribution*
706 *of Working Group I to the Sixth Assessment Report of the Intergovernmental Panel on*
707 *Climate Change*, 923–1054, https://doi.org/10.1017/9781009157896.009.

708 Gelaro, R., and Coauthors, 2017: The Modern-Era Retrospective Analysis for Research and
709 Applications, Version 2 (MERRA-2). *J. Climate*, **30**, 5419–5454,
710 https://doi.org/10.1175/JCLI-D-16-0758.1.

711 Hartmann, D. L., and K. Larson, 2002: An important constraint on tropical cloud - climate
712 feedback. *Geophys. Res. Lett.*, **29**, 1951, https://doi.org/10.1029/2002GL015835.

713 Hu, Y., and Q. Fu, 2007: Observed poleward expansion of the Hadley circulation since 1979.
714 *Atmos. Chem. Phys.*, **7**, 5229–5236, https://doi.org/10.5194/acp-7-5229-2007.

715 Jakob, C., and G. Tselioudis, 2003: Objective identification of cloud regimes in the Tropical
716 Western Pacific. *Geophysical Research Letters*, **30**, 2082,
717 https://doi.org/10.1029/2003GL018367.

718 Jin, D., and B. P. Kirtman, 2009: Why the Southern Hemisphere ENSO responses lead
719 ENSO. *J. Geophys. Res.*, **114**, https://doi.org/10.1029/2009JD012657.

720 ——, L. Oreopoulos, D. Lee, J. Tan, and N. Cho, 2021: Cloud–Precipitation Hybrid Regimes
721 and Their Projection onto IMERG Precipitation Data. *Journal of Applied Meteorology*
722 *and Climatology*, **60**, 733–748, https://doi.org/10.1175/JAMC-D-20-0253.1.

723 Kamae, Y., H. Shiogama, M. Watanabe, T. Ogura, T. Yokohata, and M. Kimoto, 2016:
724 Lower-Tropospheric Mixing as a Constraint on Cloud Feedback in a Multiparameter
725 Multiphysics Ensemble. *Journal of Climate*, **29**, 6259–6275,
726 https://doi.org/10.1175/JCLI-D-16-0042.1.

727 Klein, S. A., and C. Jakob, 1999: Validation and Sensitivities of Frontal Clouds Simulated by
728 the ECMWF Model. *Monthly Weather Review*, **127**, 2514–2531,
729 https://doi.org/10.1175/1520-0493(1999)127<2514:VASOFC>2.0.CO;2.

730 Knutson, T., and Coauthors, 2019: Tropical Cyclones and Climate Change Assessment: Part
731 I: Detection and Attribution. *Bulletin of the American Meteorological Society*, **100**,
732 1987–2007, https://doi.org/10.1175/BAMS-D-18-0189.1.

733 Koshiro, T., H. Kawai, and A. T. Noda, 2022: Estimated cloud-top entrainment index
734 explains positive low-cloud-cover feedback. *Proc. Natl. Acad. Sci. U.S.A.*, **119**,
735 e2200635119, https://doi.org/10.1073/pnas.2200635119.

736 Loeb, N. G., and Coauthors, 2018: Clouds and the Earth's Radiant Energy System (CERES)
737 Energy Balanced and Filled (EBAF) Top-of-Atmosphere (TOA) Edition-4.0 Data
738 Product. *J. Climate*, **31**, 895–918, https://doi.org/10.1175/JCLI-D-17-0208.1.

739 ——, G. C. Johnson, T. J. Thorsen, J. M. Lyman, F. G. Rose, and S. Kato, 2021: Satellite and
740 Ocean Data Reveal Marked Increase in Earth's Heating Rate. *Geophys Res Lett*, **48**,
741 e2021GL093047, https://doi.org/10.1029/2021GL093047.

742 Lu, J., G. A. Vecchi, and T. Reichler, 2007: Expansion of the Hadley cell under global
743 warming. *Geophys. Res. Lett.*, **34**, L06805, https://doi.org/10.1029/2006GL028443.

744 Mantua, N. J., S. R. Hare, Y. Zhang, J. M. Wallace, and R. C. Francis, 1997: A Pacific
745 interdecadal climate oscillation with impacts on salmon production. *Bull. Amer.*
746 *Meteor. Soc.*, **78**, 1069–1079.

747 Meng, L., J. Liu, D. W. Tarasick, W. J. Randel, A. K. Steiner, H. Wilhelmsen, L. Wang, and
748 L. Haimberger, 2021: Continuous rise of the tropopause in the Northern Hemisphere
749 over 1980–2020. *Sci. Adv.*, **7**, eabi8065, https://doi.org/10.1126/sciadv.abi8065.

750 Myhre, G., and Coauthors, 2018: Quantifying the Importance of Rapid Adjustments for
751 Global Precipitation Changes. *Geophys Res Lett*, **45**, 11399–11405,
752 https://doi.org/10.1029/2018GL079474.

753 Norris, J. R., R. J. Allen, A. T. Evan, M. D. Zelinka, C. W. O'Dell, and S. A. Klein, 2016:
754 Evidence for climate change in the satellite cloud record. *Nature*, **536**, 72,
755 https://doi.org/10.1038/nature18273.

756 O'Gorman, P. A., R. P. Allan, M. P. Byrne, and M. Previdi, 2012: Energetic Constraints on
757 Precipitation Under Climate Change. *Surv Geophys*, **33**, 585–608,
758 https://doi.org/10.1007/s10712-011-9159-6.

759 Park, S., and C. B. Leovy, 2004: Marine Low-Cloud Anomalies Associated with ENSO. *J.*
760 *Climate*, **17**, 3448–3469, https://doi.org/10.1175/1520-
761 0442(2004)017<3448:MLAAWE>2.0.CO;2.

762 Platnick, S., and Coauthors, 2017: The MODIS Cloud Optical and Microphysical Products:
763 Collection 6 Updates and Examples From Terra and Aqua. *IEEE Transx Geosci.*
764 *Remote Sens.*, **55**, 502–525, https://doi.org/10.1109/TGRS.2016.2610522.

765 ——, and Coauthors, 2018: MODIS cloud optical properties: User guide for the collection
766 6/6.1 Level-2 MOD06/MYD06 product and associated Level-3 datasets, Version 1.1.
767 https://atmosphere-
768 imager.gsfc.nasa.gov/sites/default/files/ModAtmo/MODISCloudOpticalPropertyUser
769 GuideFinal_v1.1_1.pdf.

770 Raghuraman, S. P., D. Paynter, R. Menzel, and V. Ramaswamy, 2023: Forcing, cloud
771 feedbacks, cloud masking, and internal variability in the cloud radiative effect satellite
772 record. *Journal of Climate*, 1–38, https://doi.org/10.1175/JCLI-D-22-0555.1.

773 Rayner, N. A., D. E. Parker, E. B. Horton, C. K. Folland, L. V. Alexander, D. P. Rowell, E.
774 C. Kent, and A. Kaplan, 2003: Global analyses of sea surface temperature, sea ice,
775 and night marine air temperature since the late nineteenth century. *Journal of*
776 *Geophysical Research: Atmospheres*, **108**, 4407,
777 https://doi.org/10.1029/2002JD002670.

778 Richardson, M. T., R. J. Roy, and M. D. Lebsock, 2022: Satellites Suggest Rising Tropical
779 High Cloud Altitude: 2002–2021. *Geophysical Research Letters*, **49**,
780 e2022GL098160, https://doi.org/10.1029/2022GL098160.

781 Rossow, W. B., and R. A. Schiffer, 1991: ISCCP Cloud Data Products. *Bull. Am. Meteorol.*
782 *Soc.*, **72**, 2–20, https://doi.org/10.1175/1520-0477(1991)072<0002:ICDP>2.0.CO;2.

783 ——, and ——, 1999: Advances in Understanding Clouds from ISCCP. *Bull. Am. Meteorol.*
784 *Soc.*, **80**, 2261–2287, https://doi.org/10.1175/1520-
785 0477(1999)080<2261:AIUCFI>2.0.CO;2.

786 ——, G. Tselioudis, A. Polak, and C. Jakob, 2005: Tropical climate described as a
787 distribution of weather states indicated by distinct mesoscale cloud property mixtures.
788 *Geophysical Research Letters*, **32**, L21812, https://doi.org/10.1029/2005GL024584.

789 Santoso, A., M. J. Mcphaden, and W. Cai, 2017: The Defining Characteristics of ENSO
790 Extremes and the Strong 2015/2016 El Niño. *Rev. Geophys.*, **55**, 1079–1129,
791 https://doi.org/10.1002/2017RG000560.

792 Smith, C. J., and Coauthors, 2020: Effective radiative forcing and adjustments in CMIP6
793 models. *Atmospheric Chemistry and Physics*, **20**, 9591–9618,
794 https://doi.org/10.5194/acp-20-9591-2020.

795 Soden, B. J., and I. M. Held, 2006: An Assessment of Climate Feedbacks in Coupled Ocean–
796 Atmosphere Models. *Journal of Climate*, **19**, 3354–3360,
797 https://doi.org/10.1175/JCLI3799.1.

798 Soden, B. J., A. J. Broccoli, and R. S. Hemler, 2004: On the Use of Cloud Forcing to
799 Estimate Cloud Feedback. *J. Climate*, **17**, 3661–3665, https://doi.org/10.1175/1520-
800 0442(2004)017<3661:OTUOCF>2.0.CO;2.

801 ——, I. M. Held, R. Colman, K. M. Shell, J. T. Kiehl, and C. A. Shields, 2008: Quantifying
802 Climate Feedbacks Using Radiative Kernels. *J. Climate*, **21**, 3504–3520,
803 https://doi.org/10.1175/2007JCLI2110.1.

804 Stevens, B., S. C. Sherwood, S. Bony, and M. J. Webb, 2016: Prospects for narrowing
805 bounds on Earth's equilibrium climate sensitivity. *Earth's Future*, **4**, 512–522,
806 https://doi.org/10.1002/2016EF000376.

807 Sun, M., D. R. Doelling, N. G. Loeb, R. C. Scott, J. Wilkins, L. T. Nguyen, and P. Mlynczak,
808 2022: Clouds and the Earth's Radiant Energy System (CERES) FluxByCldTyp
809 Edition 4 Data Product. *Journal of Atmospheric and Oceanic Technology*, **39**, 303–
810 318, https://doi.org/10.1175/JTECH-D-21-0029.1.

811 Tselioudis, G., W. Rossow, Y. Zhang, and D. Konsta, 2013: Global Weather States and Their
812 Properties from Passive and Active Satellite Cloud Retrievals. *Journal of Climate*, **26**,
813 7734–7746, https://doi.org/10.1175/JCLI-D-13-00024.1.

814 ——, W. B. Rossow, C. Jakob, J. Remillard, D. Tropf, and Y. Zhang, 2021: Evaluation of
815 Clouds, Radiation, and Precipitation in CMIP6 Models Using Global Weather States
816 Derived from ISCCP-H Cloud Property Data. *J. Climate*, **34**, 7311–7324,
817 https://doi.org/10.1175/JCLI-D-21-0076.1.

818 Tseng, Y.-H., R. Ding, and X. Huang, 2017: The warm Blob in the northeast Pacific—the
819 bridge leading to the 2015/16 El Niño. *Environ. Res. Lett.*, **12**, 054019,
820 https://doi.org/10.1088/1748-9326/aa67c3.

821 Webb, M., C. Senior, S. Bony, and J.-J. Morcrette, 2001: Combining ERBE and ISCCP data
822 to assess clouds in the Hadley Centre, ECMWF and LMD atmospheric climate
823 models. *Clim Dyn*, **17**, 905–922, https://doi.org/10.1007/s003820100157.

824 Wetherald, R. T., and S. Manabe, 1988: Cloud Feedback Processes in a General Circulation
825 Model. *J. Atmos. Sci.*, **45**, 1397–1416, https://doi.org/10.1175/1520-
826 0469(1988)045<1397:CFPIAG>2.0.CO;2.

827 Williams, A. I. L., N. Jeevanjee, and J. Bloch-Johnson, 2023: Circus Tents, Convective
828 Thresholds, and the Non-Linear Climate Response to Tropical SSTs. *Geophys Res
829 Lett*, **50**, e2022GL101499, https://doi.org/10.1029/2022GL101499.

Zelinka, M. D., S. A. Klein, and D. L. Hartmann, 2012a: Computing and Partitioning Cloud Feedbacks Using Cloud Property Histograms. Part I: Cloud Radiative Kernels. *J. Climate*, **25**, 3715–3735, https://doi.org/10.1175/JCLI-D-11-00248.1.

——, ——, and ——, 2012b: Computing and Partitioning Cloud Feedbacks Using Cloud Property Histograms. Part II: Attribution to Changes in Cloud Amount, Altitude, and Optical Depth. *J. Climate*, **25**, 3736–3754, https://doi.org/10.1175/JCLI-D-11-00249.1.

——, ——, K. E. Taylor, T. Andrews, M. J. Webb, J. M. Gregory, and P. M. Forster, 2013: Contributions of Different Cloud Types to Feedbacks and Rapid Adjustments in CMIP5. *Journal of Climate*, **26**, 5007–5027, https://doi.org/10.1175/JCLI-D-12-00555.1.

——, C. Zhou, and S. A. Klein, 2016: Insights from a refined decomposition of cloud feedbacks. *Geophys. Res. Lett.*, **43**, 9259–9269, https://doi.org/10.1002/2016GL069917.

——, T. A. Myers, D. T. McCoy, S. Po-Chedley, P. M. Caldwell, P. Ceppi, S. A. Klein, and K. E. Taylor, 2020: Causes of higher climate sensitivity in CMIP6 models. *Geophysical Research Letters*, **46**, 2019GL085782, https://doi.org/10.1029/2019GL085782.

——, I. Tan, L. Oreopoulos, and G. Tselioudis, 2022: Detailing cloud property feedbacks with a regime-based decomposition. *Clim Dyn*, https://doi.org/10.1007/s00382-022-06488-7.

Zhang, B., R. J. Kramer, and B. J. Soden, 2019: Radiative Feedbacks Associated with the Madden–Julian Oscillation. *Journal of Climate*, **32**, 7055–7065, https://doi.org/10.1175/JCLI-D-19-0144.1.

Zhang, M. H., J. J. Hack, J. T. Kiehl, and R. D. Cess, 1994: Diagnostic study of climate feedback processes in atmospheric general circulation models. *J. Geophys. Res.*, **99**, 5525–5537, https://doi.org/10.1029/93JD03523.

Zhou, C., M. D. Zelinka, A. E. Dessler, and S. A. Klein, 2015: The relationship between interannual and long-term cloud feedbacks. *Geophysical Research Letters*, **42**, 10463–10469, https://doi.org/10.1002/2015GL066698.

——, ——, and S. A. Klein, 2016: Impact of decadal cloud variations on the Earth's energy budget. *Nature Geoscience*, **9**, 871–874, https://doi.org/10.1038/ngeo2828.

Zhu, P., J. J. Hack, J. T. Kiehl, and C. S. Bretherton, 2007: Climate sensitivity of tropical and subtropical marine low cloud amount to ENSO and global warming due to doubled CO2. *J. Geophys. Res.*, **112**, D17108, https://doi.org/10.1029/2006JD008174.